Proxy-Model Comparison for the Eocene-Oligocene Transition in Southern High Latitudes

Emily J. Tibbett[1*], Natalie J. Burls[2], David K. Hutchinson[3], Sarah J. Feakins[1]

[1]Department of Earth Science, University of Southern California, Los Angeles, CA, USA

[2]Atmospheric, Oceanic, and Earth Sciences Department, George Mason University, Fairfax, VA, USA

[3]Climate Change Research Centre, University of New South Wales, Sydney, Australia

*Corresponding author: E. J. Tibbett (tibbett@usc.edu)

Key points

- Air temperatures at the margins of the Antarctic continent dropped by 0 to 4°C across the Eocene Oligocene Transition.
- Southern high latitude sea surface temperatures cooled by 0 to 3°C.
- Best fit to the proxy surface air temperatures from CO_2-only runs suggest a 30% decrease in pCO_2 across the Eocene-Oligocene Transition.

Abstract

The Eocene-Oligocene Transition (EOT) marks the shift from greenhouse to icehouse conditions at 34 Ma, when a permanent ice sheet developed on Antarctica. Climate modeling studies have recently assessed the drivers of the transition globally. Here we revisit those experiments for a detailed study of the southern high latitudes in comparison to the growing number of mean annual sea surface temperature (SST) and mean air temperature (MAT) proxy reconstructions, allowing us to assess proxy-model temperature agreement and refine estimates for the magnitude of the pCO_2 forcing of the EOT. We compile and update published proxy temperature records on and around Antarctica for the late Eocene (38-34 Ma) and early Oligocene (34-30 Ma). Compiled SST proxies cool by up to 3°C and MAT by up to 4° between the timeslices. Proxy data were compared to previous climate model simulations representing pre- and post-EOT, typically forced with a halving of pCO_2. We scaled the model outputs to identify the magnitude of pCO_2 change needed to drive a commensurate change in temperature to best fit the

temperature proxies. The multi-model ensemble needs a 30 or 33% decrease in pCO_2, to best fit MAT or SST proxies respectively. These proxy-model intercomparisons identify declining pCO_2 as the primary forcing of EOT cooling, with a magnitude (200 or 243 ppmv) approaching that of the pCO_2 proxies (150 ppmv). However individual model estimates span a decrease of 66 to 375 ppmv, thus proxy-model uncertainties are dominated by model divergence.

Plain Language Summary

Antarctica was once a continent with little to no ice on it. Around 34 million years ago Antarctica developed its first permanent ice sheet as temperatures cooled. To evaluate how much cooling occurred on and around Antarctica, we compiled evidence from the molecules left behind by ancient organisms, that carry information about temperature, as reported previously in the literature. We then compared the ancient evidence to climate model experiments which allows us to test cause and effect. Cooling is thought to be caused by a drop in carbon dioxide concentrations in the atmosphere, and we tested how much carbon dioxide levels would need to drop to explain the cooling found. Our estimates are similar to independent evidence from marine organisms for carbon dioxide concentrations.

Keywords: EOT, DeepMIP, IODP, BAYSPLINE, BAYSPAR, BAYMBT

1. Introduction

The Eocene-Oligocene Transition (EOT) spans 34.4 to 33.7 Ma (Coxall & Pearson, 2007; Hutchinson et al., 2021; Katz et al., 2008) and marks the growth of permanent ice sheets on Antarctica (McKay et al., 2022). This transition includes a two-step increase in benthic foraminiferal $\delta^{18}O$ by 1.2‰ (Westerhold et al., 2020). The first step increase in $\delta^{18}O_{benthic}$ is harder to identify and does not appear in all records relative to the second step, referred to as the Earliest Oligocene Isotope Step (Hutchinson et al., 2021), which is an increases in $\delta^{18}O_{benthic}$ of 0.7‰ or more denoting the expansion of the Antarctic ice sheet. Estimates for the size of the ice sheet based on the benthic $\delta^{18}O$ signal suggest an ice sheet 60-130% of the modern East Antarctic Ice Sheet (Bohaty et al., 2012b; Lear et al., 2008). This transition is marked by

a decrease in pCO_2 (Rae et al., 2021), temperature (Coxall & Pearson, 2007; Hutchinson et al., 2021; Lear et al., 2008; Liu et al., 2009), and sea level (Houben et al., 2012; Miller et al., 2020). An early hypothesis for the growth of permanent ice sheets on Antarctica was that gateway openings at the Drake Passage and Tasman Gateway led to thermal isolation of Antarctica (Kennett, 1977). Several ocean-only or intermediate complexity climate models suggest that the opening or deepening of the Southern Ocean gateways could have a local cooling effect close to the Antarctic coast (Sauermilch et al., 2021; Sijp et al., 2009). However, the accumulating proxy records and coupled climate modelling experiments have indicated that the gateway hypothesis does not fully explain the global cooling experienced at the EOT (e.g., Hutchinson et al., 2021; Lauretano et al., 2021). Ocean circulation proxy reconstructions indicate that the timing does not match the proposed mechanism. Deep water currents through the Tasman Gateway were first established around 30 Ma (Scher et al., 2015), i.e., after the EOT. For the Drake Passage, full opening may have occurred even later, in the Miocene (Dalziel et al., 2013).

A growing consensus is that a decrease in pCO_2 across the EOT is the primary driver for the EOT and temperature decrease globally (DeConto & Pollard, 2003; Goldner et al., 2014; Hutchinson et al., 2021; Lauretano et al., 2021; Pagani et al., 2011). Previous model proxy comparisons indicating a decrease in pCO_2 by 40% can explain the global temperature shift (Hutchinson et al., 2021). Recent pCO_2 compilations (Rae et al., 2021) constrain a decrease in pCO_2 from 980 to 830 ppmv, a 16% decrease, based on the boron isotope proxy (Anagnostou et al., 2016, 2020; Henehan et al., 2020; Pearson et al., 2009) and from 660 to 520 ppmv from alkenones, a 27% decrease, across the EOT (Pagani et al., 2005, 2011). Both proxies converge on the magnitude of the decrease being just 140-150 ppmv between the late Eocene and the early Oligocene, and when averaging across both proxies there is roughly a 25% decrease across the EOT (Rae et al., 2021). Although carbon dioxide has been established as the leading cause, additional feedbacks are invoked from both the ice-albedo feedback and gateway-induced changes to deep-water formation (Goldner et al., 2014). Several coupled climate model studies have found a shift from South Atlantic to South Pacific deep-water formation across the EOT due to Southern Ocean

gateway opening (Kennedy et al., 2015; Toumoulin et al., 2020). Furthermore, deep water circulation proxies suggest that there was an expansion of North Atlantic Deep Water formation around the EOT (Coxall et al., 2018), supported by paleogeographic and modelling evidence of the Arctic becoming isolated from the North Atlantic (Hutchinson et al., 2019; Vahlenkamp et al., 2018). These studies suggest that ocean gateway and ice sheet changes could be involved in driving the observed changes at the EOT, although declining pCO_2 is the only mechanism proven to cause global cooling.

Climate models allow the drivers of change to be tested. Inter-model differences in boundary conditions (e.g., continental configuration) and parameterization schemes can lead to different outcomes. Multi-model comparisons can test the robustness of hypotheses for the transition to these differences in model formulation. One surprising feature of climate model experiments, is the finding of a smaller decrease in surface air temperatures at higher latitudes in comparison to mid-latitudes across the EOT (Kennedy-Asser et al., 2020). Model experiments also indicate Southern Ocean sea surface temperatures (SSTs) cooled more than the land at the same latitude. SST proxies indicate a global average cooling of 2.5°C across the EOT and regional differences in cooling ranging from 0 to 8°C (Hutchinson et al., 2021). Compiled global land surface mean air temperature (MAT) proxy records suggest a global mean cooling of 2.3°C with latitudinal and regional differences in cooling from 0 to 8°C (Hutchinson et al., 2021). However, proxy records are concentrated in northern mid-latitudes with limited records from the Southern Hemisphere and few from Antarctica. The sparse coverage of proxy records in the Southern Hemisphere and from Antarctica has hampered past efforts to evaluate model outputs.

We now have more temperature records to assess the magnitude of the land and sea temperature shift across the EOT surrounding the Southern Ocean. For example, there are now *br*GDGT-based temperature estimates on both sides of the Southern Ocean from Prydz Bay (Tibbett et al., 2021a) and South Australia (Lauretano et al., 2021). We add these new records to compiled proxies and multi-model experiments for the EOT (compiled by Hutchinson et al., 2021). Hutchinson et al., (2021) compiled proxy data globally, whereas we take a more in-depth look at the southern high latitudes (>45ºS) including Antarctica. For this

proxy-model comparison, we update the proxy compilation using the latest calibrations and we update proxies onto a comparable timescale. In contrast to the recent high latitude study by Lauretano et al., (2021) that compared to a single climate model, we compare to the full suite of model experiments as in Hutchinson et al., (2021). While the individual model experiments generally used a halving of carbon dioxide to force a large EOT response, we scale the model experiments to identify the pCO_2 forcing required to better reproduce the temperature anomaly across the transition observed in the proxy data in the high southern latitudes. The focused multi-proxy, multi-model high latitude comparison allows us to identify sub-regional differences in the proxies and in the climate model experiments to reach new understanding of the forcing and response during the Eocene-Oligocene Transition on and around Antarctica.

2. Methods

2.1. Proxy data

Proxy temperature records were collected south of 45°S (**Figure 1a**) based on paleolatitudes for the late Eocene (38 to 34 Ma) and early Oligocene (34 to 30 Ma) collating records from land and sea for MAT and SST (**Figure 1b,c**). Paleocoordinates were reconstructed using the modern day drilling coordinates and GPlates (Müller et al., 2018) to reconstruct paleolatitude and paleolongitudes at 34 Ma. Proxy methods for the temperature reconstructions are noted and where appropriate the data were recalibrated to the latest methods for compatibility within the compilation (as described in the following sections on MAT and SST). Age models were updated to the GTS2012 age model (Gradstein et al., 2012) for comparability in the 4 Ma windows bracketing the EOT transition. Each of these updates (location, proxy calibration and age model) can be found in the proxy synthesis (Tibbett et al., 2022a).

2.1.1. MAT

For the southern continents, reconstructions of mean annual air temperatures (MAT, **Table 1**) come from palynological analysis (Francis et al., 2008; Hunt & Poole, 2003; Macphail & Truswell, 2004; Poole et

al., 2005; Truswell & Macphail, 2009), which identifies pollen grains to plant genus or species level and constrains the climate based on known temperature and precipitation ranges of the extant species or nearest living relative (NLR) (Amoo et al., 2022; Thompson et al., 2022), as a probability density function (and central estimate) of likely climatic range (Harbert & Nixon, 2015; Hollis et al., 2019; Willard et al., 2019). The temperature compilation for the continents also includes mineral weathering via the S-index climofunction (Passchier et al., 2013, 2017) which is based on the molar ratio of Na_2O and K_2O to Al_2O released during weathering (Sheldon et al., 2002).

We also compiled records using the soil bacterial biomarkers, the branched Glycerol Dialkyl Glycerol Tetraethers (*br*GDGTs). The original MBT/CBT (Cyclization of Branched Tetraethers) index (Douglas et al., 2014) includes temperature responsive methylation, but also the cyclization of *br*GDGTs, which varies with pH complicating that paleothermometer (Weijers et al., 2007). A newer method determines the MBT'_{5Me} index based only on the methylation of *br*GDGTs, which responds to temperature (Hopmans et al., 2016), an approach available after improvement in the separation of the 5- and 6-methyl *br*GDGTs (De Jonge et al., 2014; Hopmans et al., 2016). The MBT'_{5Me} index has been calibrated to temperature (both mean annual and months above freezing) with the Bayesian regression model of the Methylation of Branched Tetraethers index (BayMBT) (Dearing Crampton-Flood et al., 2020). For both the Eocene and the Oligocene cases the MAF and MAT estimates are indistinguishable. BayMBT calibrated data are reported with the calibration to mean annual air temperature for the purposes of consistency with other mean annual air temperature (MAT) proxies and the reporting conventions for proxy-model comparison. However we will return to the seasonal question and the latest calibrations to months above freezing (MAF), based on the understanding that soil microbial communities are unlikely to be active below freezing (Deng et al., 2016; Weijers et al., 2007, 2011), at the end of the discussion. All BayMBT records, from marine drill cores, were screened for additional indices (e.g., BIT and $\#Rings_{tetra}$) that can denote confounding factors similar to tests in Tibbett et al., (2022b), as no aquatic overprinting was identified for the records, none were excluded. The WW7 record is from a terrestrial peat deposit and therefore is not at

risk for marine overprinting. The MBT/CBT record cannot be recalibrated using BayMBT due to the lack of separation of the 5 and 6 methyl isomers but is retained. We have one instance of a peat-based temperature estimate (Lauretano et al., 2021) reported using the MBT_{peat} calibration (Naafs et al., 2017) that was recalibrated using BayMBT (Dearing Crampton-Flood et al., 2020), with no significant change in estimated MAT.

Table 1. Mean annual air temperature proxy compilation for late Eocene (38-34 Ma) and early Oligocene (34-30 Ma).

				Late Eocene MAT		Early Oligocene MAT		O-E	
Location	Lat	Long	Proxy	Mean (ºC)	1σ (ºC)	Mean (ºC)	1σ (ºC)	Δ(ºC)	Reference
739, 742,1166	-67.3	75.1	BayMBT	11.0	2.0	6.8	2.6	-4.2	Tibbett et al., 2021b
739, 742,1166	-67.3	75.1	S-index	10.4	1.0	8.1	0.5	-2.3	Passchier et al., 2017
CIROS-1 CRP Sites 2/3	-77.7	163.5	S-index	8.7	1.2	7.8	1.3	-0.9	Passchier et al., 2013
U1356	-63.3	136.0	S-index			8.9	1.2		Passchier et al., 2013
WW7	-38.2	147.1	BayMBT	23.3	1.6	20.2	1.2	-3.1	Lauretano et al., 2021 recalibrated using BayMBT
Seymour Island	-64.4	-56.8	MBT/CBT*	12.2	2.3				Douglas et al., 2014
King George Island, Dragon Glacier	-62.1	-58.9	Pollen**	12.0					Hunt & Poole, 2003; Poole et al., 2005
King George Island, Fossil Hill	-62.1	-58.9	Pollen**	13.3					Poole et al., 2005
McMurdo	-77.6	166.4	Pollen**	13.0					Francis et al., 2008
King George Island, South Sheltand Island	-62.0	-58.4	Pollen**	13.4					Francis et al., 2008
1166	-67.3	75.1	Pollen**	12.0					Macphail & Truswell, 2004; Truswell & Macphail, 2009
CRP-3	-77.0	163.7	Pollen**			6.5			Francis et al., 2008
SHALDRIL	-63.8	-54.7	BayMBT	6.9	0.5				Tibbett et al., 2022c
696	-61.8	-42.9	NLR	11.9	1.8	11.2	1.0	-0.7	Thompson et al., 2022
1172	-43.9	158.3	NLR	11.7	1.7	11.9	1.7	+0.2	Amoo et al., 2022

* Douglas et al., (2014) also reported MBT′/CBT, excluded as unrealistically warm. **Pollen-based temperature estimates are reported here as MAT. Standard deviations represent timeseries variability. Latitude and longitude are reported for present positions and are reported to 0.1° resolution.

2.1.2. SST

Southern high latitude SST records (**Table 2**) are from the archaeal membrane lipid TEX_{86} index (Douglas et al., 2014; Hartman et al., 2018; Lauretano et al., 2021; Tibbett et al., 2021a) which is based on the relationship between SST and the degree of cyclization of isoprenoidal GDGTs (isoGDGTs) produced by Crenarchaeota (Schouten et al., 2002). Additional SST records include the haptophyte algal biomarker $U^{k'}_{37}$ index (Houben et al., 2019; Liu et al., 2009; Pagani et al., 2011; Plancq et al., 2014), which in the Eocene and Oligocene were produced by the *Reticulofenestra* (Henderiks & Pagani, 2008), *Cyclicargolithus* or *Dictyococcites* (Brassell, 2014). The $U^{k'}_{37}$ index SST relationship is based on the proportion of di- and tri-unsaturated C_{37} alkenones (Prahl & Wakeham, 1987; Sikes et al., 1997; Sikes & Volkman, 1993). Carbonate clumped isotopes Δ_{47} values measured on shallow coastal bivalves were also included as SST proxies (Douglas et al., 2014; Petersen & Schrag, 2015) since "clumped" ^{18}O-^{13}C is responsive to temperature (Ghosh et al., 2006). For Douglas et al., 2014 the TEX_{86} SSTs were reevaluated using BAYSPAR (Bayesian, Spatially-Varying Regression calibration for TEX_{86}) (Tierney & Tingley, 2014) with a prior of 13°C and a standard deviation of 15°C. Other TEX_{86} records from the Southern Ocean were either originally calibrated with BAYSPAR (Hartman et al., 2018; Lauretano et al., 2021; Tibbett et al., 2021a), or were recently reevaluated using BAYSPAR (Lauretano et al., 2021) with priors ranging from 12 to 21°C and a standard deviation of 20°C. The $U^{k'}_{37}$ records were reinterpreted using the latest BAYSPLINE (B-spline fit with a Bayesian regression) calibration (Tierney & Tingley, 2018). Other published records in the region based on $\delta^{18}O_{benthic}$ methods (Zachos et al., 1996) were not included in the SST compilation due to diagenetic recrystallization that leads to cold biases in reported temperatures (e.g., Raymo et al., 2018).

Table 2. Sea surface temperature proxy compilation for the late Eocene (38-34 Ma) and early Oligocene (34-30 Ma)

	l. Eocene SST	e. Oligocene SST	O-E

Site	Lat	Long	Proxy	Mean (ºC)	1σ (ºC)	Mean (ºC)	1σ (ºC)	Δ (ºC)	Reference
739, 742, 1166	-67.3	75.1	BAYSPAR	12.6	1.7	10.4	1.1	-2.2	Tibbett et al., 2021b
689	-64.5	-3.1	Δ_{47}	13.3	5.0	12.0	0.9	-1.3	Petersen & Schrag, 2015
511	-51.0	-47.0	BAYSPAR	15.7	2.1	13.1	1.0	-2.6	Houben et al., 2019 * Lauretano et al., 2021
511	-51.0	-47.0	BAYSPLINE	17.6	2.1	10.8[x]	2.5	-6.8	Houben et al., 2019[x],[#],**
511	-51.0	-47.0	BAYSPLINE	18.2	2.5	10.7[x]	0.8	-7.5	Liu et al., 2009; Plancq et al., 2014, from Elsworth et al., 2017[x],**
277	-52.2	166.2	BAYSPAR	26.6	1.1	24.0	0.4	-2.6	Pagani et al., 2011,* Lauretano et al., 2021
277	-52.2	166.2	BAYSPLINE	25.4	1.8	23.1	2.0	-2.3	Pagani et al., 2011 **
1172	-43.9	158.3	BAYSPAR	20.5	1.1	20.5	0.9	0	Houben et al., 2019 * from Lauretano et al., 2021
U1356	-63.3	136.0	BAYSPAR			18.7	2.0		Hartman et al., 2018
Seymour Island	-64.4	-56.8	BAYSPAR	13.5	2.1				Douglas et al., 2014 *
Seymour Island	-64.4	-56.8	Δ_{47}	12.9	0.7				Douglas et al., 2014

*TEX_{86} recalibrated from original publication with BAYSPAR. ** $U^{k'}_{37}$ recalibrated with BAYSPLINE. Standard deviations represent timeseries variability. Latitude and longitude are reported for present positions and are reported to 0.1° resolution. [#] DSDP Site 511 SST reconstruction (Houben et al., 2019) updated with ages from Lauretano et al., (2021). [x] Site 511 has two BAYSPLINE entries, both with anomalous Oligocene cooling, that are excluded from the proxy-model comparison.

2.1.3. Proxy Uncertainty

Proxy uncertainty varies by proxy and is defined in the original calibration studies for each proxy, although the uncertainty is necessarily less well known in application to the past. For the GDGT-based proxies, SST and MAT values estimated by BAYSPAR and BayMBT respectively, carry one standard deviation calibration uncertainty ca. 4°C. The standard error reported for the linear regression of MBT/CBT to temperature is 5.5°C (Weijers et al., 2011). The $U^{k'}_{37}$ BAYSPLINE calibration carries a standard deviation of ca. 4°C (Tierney & Tingley, 2018). For clumped isotopes uncertainties come from instrument error, sample heterogeneity and accuracy summarized as 2.5°C in the Seymour Island study (Douglas et al., 2014). Pollen temperatures generated from nearest living relative analysis are reported to have a standard deviation of 2 to 3°C (Amoo et al., 2022; Thompson et al., 2022). For S-index the reported calibration standard deviation is 3.6°C (Sheldon et al., 2002). The approaches used to quantify

uncertainty do vary between calibration approaches, with the error propagation captured rigorously in the bayesian calibrations and may be underreported in other cases. Beyond calibration uncertainty, the uncertainty around the central estimate for each timeslice is dependent upon the number of data points and the variability and length of the window chosen. For the intervals chosen here we report the standard deviation for each timeseries representing the variability around the means for each timeslice (**Table 1 and 2**). The selection of a longer time window can lead to more time averaging and thus dampening of the magnitude of the transition, as will be explored in the results.

At sites with multi-proxy reconstructions, we can assess the direction and magnitude of proxy-proxy discrepancy at each site and for each timeslice, and we can test sensitivity to the exclusion of single reconstructions and proxy types in addition to the comparison of MAT versus SST proxies which are also independent assemblages of data. As an example for land proxies, archived in marine sediments at Prydz Bay the difference between the S-index and BayMBT is up to 4°C. The S-index is cooler due to inferred higher elevation sourcing of the rock-erosion proxy (S-index) versus the lower elevation (warmer) sourcing of soil microbial biomarkers (Tibbett et al., 2021a). For the SST proxies, at Site 277 both BAYSPAR and BAYSPLINE agree within error with cooling of 2.2 and 2.6°C respectively across the EOT (Lauretano et al., 2021; Pagani et al., 2011). These two proxies agree despite different producers: haptophyte algae which produce alkenones (for the $U^{k'}_{37}$ index and BAYSPLINE) are primary producers and are found in the photic zone (Popp et al., 2006; Volkman et al., 1980), whereas Thaumarchaeota (producers of *iso*GDGTs used for TEX_{86} and BAYSPAR) were more abundant in the subsurface of the Southern Ocean (Kalanetra et al., 2009), raising the possibility that proxy-proxy discrepancies may in part arise from different depth habitats when there is a vertical gradient in ocean temperatures. Offsets between temperature proxies have also been linked to the problem of lateral advection of alkenones leading to cold biases and older ages of alkenones in cold current settings (Mollenhauer et al., 2003). The largest offset of alkenones from modern SSTs in the modern global oceans has been reported from the SE margin of South America with a cold bias of up to 8°C (Tierney and Tingley, 2018). In the same margin,

223 at DSDP Site 511 alkenones record an anomalous cooling of ~8°C (Houben et al., 2019) interpreted with
224 BAYSPLINE, whereas at the same site the TEX_{86} proxy interpreted with BAYSPAR records ~3°C
225 cooling (Lauretano et al., 2021) consistent with other high southern latitude EOT reconstructions. The
226 correspondence of the cold offset of alkenones relative to TEX_{86} and $\delta^{18}O_{benthic}$ records (Houben et al.,
227 2019) with the known magnitude of alkenone biases relative to modern SSTs along the Southeastern
228 South American margin (Tierney and Tingley 2018) suggest that similar biases were at play in this
229 location in the past. We exclude the anomalous cooling inferred from alkenones (BAYSPLINE) at Site
230 511 (**Table 2**) from the proxy-model comparison, and we perform a sensitivity test for this worst case
231 scenario proxy-proxy disagreement (**Section 4.1**).

232 **2.2. Models**

233 We re-use the ensemble of model experiments gathered onto a uniform grid used in the HadCM3BL
234 model by Hutchinson et al., (2021). The initial grid resolution can be found in the original papers (**Table**
235 **3**) for each model simulation (Baatsen et al., 2020; Goldner et al., 2014; Hutchinson et al., 2018, 2019;
236 Ladant et al., 2014a, 2014b; Sijp et al., 2016; Z. Zhang et al., 2012, 2014). The compiled experiments
237 include two broad groupings 4x CO_2 (Eocene-like high pCO_2) and 2x CO_2 (Oligocene-like low CO_2) each
238 run without ice sheets to isolate only the effects of changing pCO_2 (**Table 3**). Additional model runs were
239 included for a subset of models to compare other EOT drivers which included the paleogeography
240 changes across the EOT (CESM_H, GFDL CM2.1, HadCM3BL, FOAM, UViC, NorESM-L), and the
241 inclusion of an ice sheet (CESM_H, FOAM, HadCM3BL) (**Table 3**). In addition, an ensemble mean for
242 each comparison was obtained by averaging across the model simulations. The pCO_2 (2x vs 4x),
243 paleogeography (pre-EOT vs post-EOT), and ice (no ice vs ice sheet) compared parameters can be found
244 in **Table 3**. More detailed information on the boundary conditions for each simulation used can be found
245 in the supplement (**Text S1**). In addition, all models used in each comparison were averaged to generate
246 an ensemble mean for each analysis performed. A correction was applied to the NorESM-L model
247 simulation that originally used a pCO_2 drop from 980 to 560 ppmv. This was scaled by Hutchinson et al.,

(2021) to match the 4x/2x simulations (50% reduction in pCO_2 across the EOT) in the other models and maintained here. The summary of the model parameters can be found in **Table 3** and detailed model run information for each of the models in the ensemble can be found in Hutchinson et al., (2021; and references therein). Here, we scale the model outputs to the proxy temperature differences to identify the pCO_2 decrease across the EOT. As in the approach of Hutchinson et al., (2021), the 2x-4x pCO_2 (Oligocene-Eocene) model results were scaled by a constant, ranging from 0 to 2, with 1 representing a 50% decrease (2x-4x pCO_2), from the initial models, to determine the forcing required to achieve the best fit between the proxies and the model for each simulation. Although commonly referred to as surface air temperature (SAT) in the model literature, we refer to land surface mean air temperatures as MAT, to be consistent with the proxy literature.

Table 3. Model simulation parameters compared for each set of paired model runs

Model	pCO_2 (ppmv) model simulations		ice model simulations (volume km^3)		paleogeography model simulations		Reference
	Eocene	Olig.	Eocene	Olig.	Eocene	Olig.	
CESM_B	1120	560	no ice		38 Ma (no paleogeography changes between timeslices)		(Baatsen et al., 2020)
CESM_H	1120	560	no ice	$20.3x10^6$	Drake and Tasman closed	Drake and Tasman open	Goldner et al., 2014
FOAM	1120	560	no ice	$25.0x10^6$	WA below sea level	WA above sea level	Ladant et al., 2014a; Ladant., et al., 2014b
GFDL CM2.1	800	400	no ice		Arctic gateway open	Arctic gateway closed	Hutchinson et al., 2018, 2019
HadCM3BL	1120	560	no ice	$17.0x10^6$	Priabonian reconstruction	Chattian reconstruction	Kennedy et al., 2015
NorESM-L	1120 (980 initial)	560	no ice		35 Ma reconstruction	33 Ma reconstruction	Zhang et al., 2012, 2014
UViC	1600	1600	no ice		Drake closed	Drake Open	Sijp et al., 2016

Three sets of model simulations were compared pCO_2 high vs low (4x vs 2x), no ice vs ice simulations, and paleogeographic simulations pre-EOT and post-EOT. The simulations outside of the pairings do not have the same conditions (**Text S1**). For models with more than one parameter all other factors held constant. NorESM-L was scaled to 1120 ppmv. For the ice/no ice runs pCO_2 is held constant at 560 ppmv. For the paleogeography runs the pCO_2 for both pre- and post-EOT is 1120 ppmv for CESM_H, 560 ppmv for FOAM, HadCM3BL and NorESM-L, 800 ppmv for GFDL CM2.1, and 1600 ppmv for UViC. Drake = Drake Passage, Tasman = Tasman Gateway, WA = West Antarctica, Olig = Oligocene.

Where land temperature proxies (e.g., soil bacterial biomarkers or soil weathering indicators) were recovered from marine sedimentary archives, we inferred sourcing from the adjacent continent. Source regions were defined on the adjacent land mass, averaging the modelled surface temperatures within an area reflective of Antarctic drainage basins. The source region was adjusted for the Prydz Bay BayMBT record as the organic material is likely sourced from the lowland soils (Tibbett et al., 2021a) with sourcing based on topography reconstruction at 34 Ma (Paxman et al., 2019). The Oligocene source region was adjusted for land proxy records from Prydz Bay and from the Ross Sea as ice growth means they were likely limited to coastal sourcing (Van Breedam et al., 2022), while records from Wilkes Land were not limited to the coast as the East Antarctic Ice Sheet was determined to be further inland (Paxman et al., 2018).

For SST proxies we assume they capture temperatures in the overlying water column at the marine core site and thus compare to the nearest grid point within the model. In cases where marine archives appeared to plot "on land" due to modelled coastline imprecision, we obtained model comparison points from the nearest ocean grid cell for comparison to the marine core derived SST proxies. The proxy-model intercomparison differences are expressed as root mean square error (RMSE) (**Equation 1**) with n as the number of proxies. This was assessed for each model scenario (Eocene and Oligocene) and the difference between the two.

$$RMSE = \sqrt{\frac{\sum_{i=1}^{n}(model-proxy)^2}{n}} \quad (1)$$

2.2.1 Sensitivity to proxy spatial coverage and model heterogeneity

To evaluate how the availability of additional proxy data might potentially improve comparisons with climate models, we performed a model sensitivity test, to an increasing number of constraints, while also illuminating the existing model limitations through model-model comparisons. First, we assigned one "perfect" model simulation as having the "true" temperature and using the same proxy sampling site locations as used in our initial proxy-model comparison we compared to each of the other models to

evaluate the error. We then modeled the effect of adding all possible marine grid cells from 45°S to the Antarctic coastline for SST (n=710) and all possible land grid cells (n=960) from 60°S to 90°S for MAT comparisons. This type of approach helps to constrain uncertainties that derive from inter-model differences, which are hidden by the model ensemble approach.

3. Results

3.1. Temperature change in the proxies

The compiled temperature proxies' distributions (**Figure 1a**), and timeseries are presented for MAT (**Figure 1b**) and SST (**Figure 1c**). Although the EOT cooling is hidden by the spread of temperatures across latitudes (**Figure 1b,c**) after parsing the data by region and calculating the cooling anomalies relative to the Eocene, the EOT cooling pattern emerges more clearly (**Figure 1d,e**) as a significant shift in regional climate, that is linked to the global features of forcing and ice volume and deep ocean temperature represented by $\delta^{18}O_{benthic}$ (**Figure 1f**). While the details of each timeseries have been explored in the original publications, here we summarize the data for individual proxy and sites, for MAT (**Table 1**) and SST proxies (**Table 2**) for the 4 Ma windows bracketing the EOT. We use the mean values for the late Eocene (38-34 Ma) and early Oligocene (34-30 Ma) for the proxy-model comparisons, and, thus we are able to make use of records that only constrain one or either time period as well as those that span the transition.

3.1.1. Time-averaging of variable timeseries

Averaging may attenuate the magnitude of EOT cooling, for example where a rebound in temperature occurs post-EOT (Bohaty et al., 2012a; Tibbett et al., 2021b) perhaps linked to a rebound in pCO_2 (Pearson et al., 2009, Anagnostou et al., 2020). At Prydz Bay, cooling at the EOT was reported to be 5°C and 4°C for MAT and SST respectively (Tibbett et al., 2021a), but by averaging across the bracketing 4 Ma windows (38-34 and 34-30 Ma), the early Oligocene to late Eocene cooling is 4.2°C and 2.2°C for SST and MAT respectively – i.e., averaging dampens the calculated cooling by 30-45%. To assess sensitivity of the pCO_2 scaling to the selected window length we compared the effects of averaging 4, 2

316 and 1 Ma pre- and post-EOT. The MAT RMSE for 4 Ma averages ranged from 1.38 to 2.34°C with a
317 pCO_2 decrease of 11 to 30%. Using a 2 Ma window the RMSE ranged from 1.38 to 2.44°C with a pCO_2
318 decrease of 6 to 29% and for 1 Ma the RMSE ranged from 1.58 to 2.55°C with a pCO_2 decrease of 17 to
319 40%. The SST RMSE for 4 Ma averages ranged from 0.90 to 1.45°C with a pCO_2 decrease of 21 to 46%.
320 Using a 2 Ma window the RMSE ranged from 0.52 to 0.80°C with a pCO_2 decrease of 18 to 44% and for
321 1 Ma the RMSE ranged from 1.28 to 2.19°C with a pCO_2 decrease of 32 to 70% (**Supplemental Table**
322 **S6 and S7)**. As we saw no significant improvement for both MAT and SST with other windows, we
323 maintain the 4 Ma windows to best capture proxy availability.

324 ### 3.2. Temperature change in the model simulations

325 #### 3.2.1. pCO_2 model simulations

326 To compare the model simulations for the Antarctic the MAT was limited to >60°S and for SST >45°S.
327 The Antarctic temperature change between the Oligocene and Eocene model simulations reflects a 50%
328 decrease in pCO_2. For the MAT model simulations the CESM_B (O-E) temperature difference ranges
329 from -6.4 to -2.3°C with a mean of -4.0°C, for CESM_H it ranges from -6.3 to -1.9°C with a mean of -
330 3.9°C, GFDL CM2.1 ranges from -9.8 to -3.9°C with a mean of -6.6°C, HadCM3BL ranges from -15.0 to
331 +4.5°C with a mean of -2.4°C, FOAM ranges from -6.5 to -2.7°C with a mean of -4.3°C, NorESM-L
332 ranges from -6.7 to 0.0°C with a mean of -3.3°C, and the ensemble mean of the 6 models (excluding
333 UViC as there were no simulations for a change in pCO_2) ranges from -7.3 to -2.1°C with a mean of -
334 4.1°C. The models exhibit an average decrease of -4.1°C for MAT from the Eocene to the Oligocene for
335 the 50% decrease in pCO_2 simulated for the Antarctic. For SST the CESM_B Antarctic temperature
336 change between the Oligocene and Eocene timeslice ranges from -4.4 to -1.8°C with a mean of -3.1°C,
337 for CESM_H it ranges from -4.8 to -1.9°C with a mean of -3.3°C, GFDL CM2.1 ranges from -9.6 to -
338 3.8°C with a mean of -5.2°C, HadCM3BL ranges from -4.3 to +4.4°C with a mean of -1.2°C, FOAM
339 ranges from -7.5 to -1.9°C with a mean of -3.7°C, NorESM-L ranges from -3.7 to +0.4°C with a mean of
340 –1.6°C, and the ensemble mean of the 6 models, excluding UViC, ranging from -9.5 to -0.5°C with a

341 mean of -3.2°C. For the SST 50% decrease in pCO_2 model simulations, the average decrease in
342 temperature for the Antarctic from the Eocene to Oligocene is -3.0°C.

343 **3.2.2. Ice sheet model simulations**

344 Following the same geographic constraints as above we report the model temperature difference between
345 the no ice (Eocene) and ice sheet (Oligocene). For CESM_H the temperature ranges from -41.1 to +1.1°C
346 with a mean of -12.0°C, HadCM3BL ranges from -37.2 to +6.6°C with a mean of -11.2°C, FOAM ranges
347 from -37.4 to +3.2°C with a mean of -14.7°C, and the ensemble mean ranges from -37.6 to +0.5°C with a
348 mean of -13.3°C. For SST, CESM_H ranges from -8.8 to +1.6°C with a mean of -1.2°C, HadCM3BL
349 ranges from -2.4 to +3.3°C with a mean of -0.3°C, FOAM ranges from -6.0 to +2.7°C with a mean of
350 +0.1°C, and the ensemble mean ranges from -8.8 to +1.5°C with a mean of -0.8°C. The average change in
351 temperature across the 3 model simulations, excluding the ensemble mean, is -12.6°C and -0.5°C for
352 MAT and SST respectively.

353 **3.2.3.Paleogeography model simulations**

354 The model simulation temperature difference between the pre-EOT and post-EOT paleogeographies vary
355 by model. For MAT CESM_H ranges from -1.9 to +3.7°C with a mean of +0.1°C, GFDL_CM2.1 ranges
356 from +0.6 to +2.2°C with a mean of +1.4°C, HadCM3BL ranges from -9.6 to +19.1°C with a mean of
357 +1.9°C, FOAM ranges from -5.0 to +2.2°C with a mean of -0.3°C, UviC ranges from -2.0 to +1.3°C with
358 a mean of -0.8°C, NorESM-L ranges from -2.4 to +1.4°C with a mean of -0.1°C, and the ensemble mean
359 it ranges from -2.6 to +3.4°C with a mean of +0.4°C. For SST CESM_H ranges from -2.0 to +1.5°C with
360 a mean of -0.3°C, GFDL_CM2.1 ranges from -0.6 to +3.0°C with a mean of 1.2°C, HadCM3BL ranges
361 from -2.3 to +4.5°C with a mean of +1.5°C, FOAM ranges from -4.4 to +1.8°C with a mean of -1.2°C,
362 UviC ranges from -4.2 to +7.0°C with a mean of -0.5°C, NorESM-L ranges from -3.2 to 1.9°C with a
363 mean of -0.4°C, and the ensemble mean ranges from -3.5 to +2.6°C with a mean of +0.1°C. The average
364 change across the EOT, excluding the ensemble mean, comparing the paleogeography runs is +0.1°C for
365 SST and +0.4°C for MAT.

366 **3.3. Proxy-model temperature comparison**

3.3.1. Temperature comparison within "pCO_2 runs" without an ice sheet

For the pCO_2 runs, the RMSE for the MAT ranges from 4.6 to 7.9°C for the Eocene, 5.0 to 7.3°C for the Oligocene, and 2.3 to 3.6°C for the difference comparison (**Figure 2 and Figure S1**). The RMSE for the SST ranges from 4.6 to 8.7°C for the Eocene, 5.2 to 9.4°C for the Oligocene, and 1.2 to 3.5°C for the temperature comparison (**Figure 3 and Figure S3**). The best fit for the Eocene data is CESM_B for both MAT and SSTs (4.6°C); however, for MAT CESM_H and GFDL CM2.1 also had an RMSE of 4.6°C as well as GFDL CM2.1 for SST. All three models for MAT had the same RMSE for the Oligocene timeslice which was the lowest RMSE (5.7°C) and CESM_B had the lowest for SSTs (5.2°C). The lowest RMSE for the 2x-4x pCO_2 comparison comes from FOAM of 2.4°C for MAT and for SSTs the lowest RMSE was 1.2°C from HadCM3BL. Although they have the best fit to the data this would imply a higher pCO_2 decrease given the difference between the Eocene and Oligocene runs is a halving of pCO_2. The ensemble mean RMSE, for a halving of pCO_2, is 2.3°C and 1.6°C for MATs and SSTs respectively.

3.3.2. Temperature comparison with the "ice sheet" runs

For the ice sheet comparison only 3 models were used (CESM_H, HadCM3BL, and FOAM) as well as the ensemble mean. The RMSE for MAT ranged from 7.9 to 10.4°C for the Eocene, 10.5 to 15.4°C for the Oligocene, and 2.7 to 8.1°C for the ice-no ice comparison (**Figure 4 and Figure S4**). The RMSE for SST ranged from 8.6 to 10.3°C for the Eocene, 7.5 to 8.8°C for the Oligocene, and 1.6 to 2.5°C for the ice-no ice comparison (**Figure 4 and Figure S5**). The lowest RMSE for both MAT and SST for the difference comparison is HadCM3BL. FOAM has the highest RMSE across all three time slices for SST. The Eocene MAT no ice runs have a higher RMSE (average of ~9°C when excluding the ensemble mean) compared to the MAT Eocene pCO_2 run RMSE (average of ~6°C excluding the ensemble mean) which are run at a higher *p*CO2 (800-1120 ppmv versus 560 ppmv for Eocene ice runs) indicating that a high pCO_2 is needed to better reflect Eocene temperatures. For the Oligocene there are substantial proxy-model discrepancies (high RMSE) for MAT. Proxies confidently identify MAT above freezing, whereas

391 the climate models forced with a large difference between the ice and no ice runs yields, as high as -40°C
392 (**Section 3.2.2**), too large a cooling compared to proxies.

393 ### 3.3.3. Temperature comparison within the "Paleogeography" runs

394 Paleogeography was changed across all models except CESM_B, and to isolate the effects of
395 paleogeography, pCO_2 was held constant between the Eocene and Oligocene runs. CESM_H, GDFL
396 CM2.1, and UViC reflect changes in ocean gateways (**Table 3**). CESM_H contrasts Tasman and Drake
397 passage closed pre-EOT and open post-EOT. GDFL CM2.1 simulations have the Arctic Gateway open
398 pre-EOT and closed post-EOT, and UViC has the Drake Passage closed pre-EOT and open post-EOT.
399 FOAM has West Antarctica above sea level in the Eocene and mostly below sea level in the Oligocene
400 representation. HadCM3BL model slight changes in continental positions from the Late Eocene to early
401 Oligocene with a small shift in latitude and longitude as well as the coastline (**Figure S6 and S7**; as well
402 as Figure S3 in Hutchinson et al., 2021). NorESM-L also models paleogeography changes; however,
403 these changes are found at latitudes ranging from 0 to 30°N with no change in the Antarctic continental
404 position or coastline between the Eocene and Oligocene timeslices (**Figure S6 and S7,** as well as Figure
405 S3 in Hutchinson et al., 2021). The RMSE for MAT ranged from 4.6 to 10.8°C for the Eocene, 2.9 to
406 8.8°C for the Oligocene, and 3.5 to 6.5°C for the difference (post-EOT-pre-EOT) comparison (**Figure 4**
407 **and Figure S6**). The RMSE for SST ranged from 4.6 to 10.3°C for the Eocene, 4.3 to 11.8°C for the
408 Oligocene, and 1.8 to 4.1°C for the difference comparison (**Figure 4 and Figure S7**). The difference
409 ensemble mean for MAT is 4.6°C and for SST is 2.3°C. The MAT for the GFDL CM2.1 run has the
410 lowest RMSE of 4.6°C for the Eocene and CESM_H has the lowest RMSE of 2.9°C for the Oligocene.
411 For the Eocene and Oligocene SST runs GFDL CM2.1 had the lowest RMSE of 4.6°C for the Eocene and
412 UViC had the lowest RMSE of 4.3°C for the Oligocene. For the difference between the paleogeography
413 for each model run the lowest RMSE was 3.5°C from UViC for MAT and 1.8°C from FOAM for SST
414 (**Figure S6 and S7**). The best fit to the Eocene data is from the model with the lowest pCO_2 of 800 ppmv
415 compared to the other models with pCO_2 of 1120 ppmv and 1600 ppmv for UViC. Most of the models

suggest a warming in MAT with regional differences (**Figure S6**). This in contrast to the proxy data which suggest temperature changes of 0 to -4°C. The model with the best fit for post/pre paleogeography is FOAM which has the most cooling regionally. To note additional regional differences UViC indicates more warming in the Pacific and Ross Sea sectors of the Southern Ocean while CESM_H suggest warming in the Atlantic and Indian Ocean sector with a cooling in the Pacific and Ross Sea sectors. This difference could be attributed to the prescribed modeled gateway opening in the Southern Ocean with CESM_H modeling the opening of Drake Passage and the Tasman Gateway and UViC modeling the opening of only Drake Passage. The overall warming trend suggests that paleogeography is not the primary driver of hemispheric cooling as previously noted (Hutchinson et al., 2021; Kennedy-Asser et al., 2020) but could impact regional differences in combination with pCO_2. It is plausible that paleogeography changes could have indirectly triggered pCO_2 changes. Two such mechanisms include a shift in the dominant basin of deep-water formation changing the ocean's ability to store carbon (Fyke et al., 2015; Speelman et al., 2009), or through land-based CO_2 weathering feedbacks triggered by the onset of the Atlantic meridional overturning circulation (Elsworth et al., 2017).

3.4. CO_2 scaling

Here we compare the updated Antarctic proxy record (rather than the global proxy data) with scaled pCO_2 to both surface air temperature and sea surface temperature. For the pCO_2 decrease calculations the assumed post-EOT pCO_2 is set at 560 ppmv, since this matches most of the models. RMSE was calculated between the 2x-4x pCO_2 runs and the Oligocene-Eocene proxies for both MAT and SST. By varying the scaling factor, we found the lowest RMSE and the best estimated decrease in pCO_2 for each model for MAT and SST proxies separately (**Figure 5**, **Table S1**). Averaging across all models (excluding the model ensemble mean), the average pCO_2 decrease is 170 ppmv for MAT and 235 ppmv for SST. This is equivalent to a 23 or 35% pCO_2 decrease when averaging all models excluding the model ensemble mean. The ensemble mean indicates a decrease of pCO_2 of 30.3 and 33.1% across the Eocene-Oligocene Transition for MAT and SST respectively, equivalent to ~200 and ~234 ppmv. The difference

441 of 3% is a measure of the proxy derived uncertainty, between two independent ensembles of proxies, used
442 to perform the scaling experiments.

443 There are however large differences between individual models. The largest decrease in pCO_2 is required
444 in the HadCM3BL (362 ppmv) and NorESM-L (375 ppmv) climate models when fitting to the proxy SST
445 data. When fitting to the smaller MAT difference, commensurately smaller changes are needed, with the
446 largest changes needed in CESM_H (221 ppmv) and FOAM (232 ppmv) when matching the shift in
447 MAT. The lowest RMSE for MAT is 1.35°C and for SST it is 0.90°C for the GFDL CM2.1 and CESM_B
448 model experiments respectively. Although the RMSE range is small, ranging from 1.4 to 2.3°C for MAT
449 and 0.9 to 1.5°C for SST, SSTs have the highest range in pCO_2 percent decrease (21.0 to 46.4%) in
450 comparison to the MATs (10.5 to 30.3%) (**Table S1**). This implies larger model discrepancy in ocean
451 conditions than on land. Overall, a much larger proportion of uncertainty derives from model rather than
452 proxy uncertainty.

453 ## 4. Discussion

454 ### 4.1. Biases in proxy temperature records

455 Land temperature proxies carry uncertainties in absolute temperatures. For the S-index the absolute
456 temperatures can be cool-biased (Sheldon & Tabor, 2009), and although attempts were made to account
457 for reworking of weathered material from older sedimentary rocks (Passchier et al., 2013, 2017),
458 temperatures were cold-biased compared to soil biomarkers (Tibbett et al., 2021a) which is attributed to
459 differing source regions. In this study we alter the source regions in the models to better represent the
460 varying source regions (**Figure S2**). The nearest living relative (NLR) approach assumes that the climate
461 tolerances of past species are similar to their modern relatives (Hollis et al., 2019) and uncertainty
462 depends on the quality of modern data and identification of fossil taxa (Utescher et al., 2014). As usual,
463 the best way to corroborate such uncertainties is through cross checks with independent data such as that
464 available from leaf traits (Pound & Salzmann, 2017) and temperature reconstructions included here

(Lauretano et al., 2021; Tibbett et al., 2021a) that support the nearest living relative results (Amoo et al., 2022; Thompson et al., 2022).

In almost all cases SST proxy-proxy agreement is good except at DSDP Site 511, on the Falkland Plateau, in the Atlantic Ocean, where the alkenones show an anomalous cooling and were excluded. Elsewhere, the proxies broadly agree thus there is likely no consistent proxy bias in terms of depth of production, seasonality or evolutionary changes not accounted for by calibration. Lateral advection of the alkenones is a likely explanation for offsets, and we note has previously led to the exclusion of data in this region from the modern datasets for the global calibration (Tierney & Tingley, 2018). Beyond the physical reasons for the offsets in the two proxies at Site 511, that are necessarily inadequately constrained for the ancient ocean, we can evaluate the numerical implications of the proxy uncertainty. As a worst-case scenario of proxy disagreement, we test inclusion of the anomalous Site 511 alkenone data. The anomalously large cooling (~8°C) leads to a large proxy-model RMSE 2.07°C and leads to the largest calculated pCO_2 decrease across the EOT (44.1%), larger than proxy estimates. Our exclusion of this outlier reduces the pCO_2 scaling to a 33.1% decrease in pCO_2, in line with proxy estimates (Rae et al., 2021) and the RMSE reduces to 1.01°C, making this the preferred choice. However, we note the low number of sites available (n=6) limits the robustness of this CO_2 scaling exercise overall.

We performed the same proxy-model temperature comparison, sequentially eliminating individual records. For SST (n=5), there was no significant improvement in RMSE other than for the removal of Site 511 BAYSPLINE (**Supplemental Table S9).** The analysis was also performed by eliminating proxy types which for SST were BAYSPAR, BAYSPLINE, and clumped isotopes (**Supplemental Table S11)**. For MAT (n=5) there was no significant improvement to the RMSE by removing individual site (**Supplemental Table S8**). For MAT, the proxy sets that were removed to evaluate the impact on the results were BayMBT, S-index, and pollen analysis (both NLR and pollen assemblage), with no notable effect (**Supplemental Table S10)**. However, we acknowledge the small number of proxies (n=6) for comparison.

To evaluate how the availability of additional marine core site SST and MAT reconstructions might improve comparisons with climate models, we performed a "perfect-model" sensitivity test, to an increasing number of constraints from the synthetic data first from the model grid cells corresponding to the proxy site locations and then from all available grid cells. Using only the "proxy sites" to compare between modelled SST values, the individual models converged on a 50% decrease in pCO_2 (**Figure S12**). For MAT, there is a larger discrepancy amongst models regarding the pCO_2 change, likely due to land boundary condition differences especially topography. We then modeled the effect of adding all possible marine grid cells from 45°S to the Antarctic coastline for SST (n=710) and all possible land grid cells (n=960) from 60°S to 90°S for MAT comparisons. For most of the models the RMSE increased slightly between the initial model comparison with the prescribed proxy sites and the use of all the model grid cells. The ensemble mean increased from 1.37 to 1.42°C for MAT and 1.09 to 1.18°C for SST (**Table S5**). Based on the minimal change in the RMSE from a low number of sites (n=6 MAT, n=6 SST) to the maximum number of grid cells (n=960 MAT, n=710 SST) it does not appear that the number of proxies is the limiting factor in proxy-model comparison. Instead, the uncertainty in our proxy-model comparisons is primarily driven by discrepancies between the model simulations in terms of the climate sensitivity to the halving of CO_2. Additionally, for MAT where the specified source region changes between the Eocene and Oligocene timeslice model differences in spatial pattern of prescribed model boundary conditions becomes a source of model spread. This analysis was therefore repeated assuming a constant surface area for the Eocene and Oligocene timeslices and the model mean then better reflect a 50% decrease using this perfect model approach. This improvement highlights a tradeoff between better representing the source regions and an additional source of model uncertainty due to the differences in topography.

4.2. Ice sheet extent and ocean circulation

Ice sheet model runs suggest SST cooling in all models with regional differences, although the RMSE is higher than in the other proxy-model comparisons **(Figure 4 and Figure S5**). Previous modeling studies

found the growth of the Antarctic ice sheet had a larger effect on SSTs than changing paleogeography (Goldner et al., 2014). The model studies show how growing ice sheets served as a positive feedback on ocean circulation changes and pCO_2 drawdown and cooling. Proxy data show the initiation of Atlantic meridional overturning circulation during the late Eocene/EOT (Coxall et al., 2018). The models used in this study have regional differences in warming and cooling around the Antarctic continent in response to the ice sheet and different feedbacks within the models, and their different boundary conditions. For example, FOAM shows warming in the Southern Ocean while CESM_H shows cooling primarily with some warming in the Indian and Pacific Ocean sectors (**Figure S5**).

The defining feature of the Eocene Oligocene Transition is the glaciation of Antarctica. The model runs used to represent the Oligocene in this comparison have prescribed ice sheet sizes ranging from $17x10^6$, $20x10^6$, and 25 $x10^6$ km^3 for HadCM3BL, CESM_H, and FOAM respectively (Goldner et al., 2014; Kennedy et al., 2015; Ladant et al., 2014a; Ladant et al., 2014b). These ice volumes correspond to ~65%, 75% and 95% of the modern Antarctic ice sheet respectively, which fall within estimates from benthic $\delta^{18}O$ that place the EAIS at 60-130% of the modern EAIS, with uncertainty due to the large range of estimates for $\delta^{18}O_{ice}$ for the Oligocene (Bohaty et al., 2012b; Lear et al., 2008). It should be noted that the range presented in the climate model are on the lower end of the ice volume estimates as the higher surface topography may have led to a larger ice sheet growth at the EOT with an estimated ice volume of $33.4x10^6$ to $35.9x10^6$ km^3 (Wilson et al., 2013). Despite the relatively small Oligocene ice sheets in the model, climate model comparisons (ice-no ice) yield too large a cooling with a decrease of -40°C in the middle of the continent (-47 to +7°C temperature change elsewhere). Likely the ice sheet contrast imposed is too great (**Figure S4**), and the problem may lie with the representation of the late Eocene.

The late Eocene included ephemeral glaciations notably the Priabonian Oxygen Isotope Maximum (PrOM) around ~37.5 Ma reaching the coastline, but not persisting (Scher et al., 2014), with glacial initiation in the Gamburtsev Mountains during the latest Eocene (Rose et al., 2013) and glacial erosion before the EOT (Carter et al., 2017; Galeotti et al., 2016). Geochemical evidence from the Kerguelen

Plateau at 33.9-33.6 Ma (Scher et al., 2011), and sedimentary records from the western Ross Sea suggest the EOT glacial expansion reached the coast at 32.8 Ma (Galeotti et al., 2016). Modeling ice sheet growth found ephemeral glaciation when pCO_2 reached a threshold of 750-900 ppm (Van Breedam et al., 2022), these pCO_2 levels were reached during the late Eocene as far as back as 40 Ma based on pCO_2 reconstructions (**Figure 1f**) (Rae et al., 2021). Therefore, the lack of ice present in the late Eocene model runs does not match the available evidence for ephemeral ice in Antarctica and may contribute to the proxy-model temperature discrepancies for the individual timeslices.

After the EOT, the use of a full ice sheet for model outputs for the Oligocene is not consistent with pollen evidence for refugial vegetation on the Antarctic Peninsula (Anderson et al., 2011). Proxies record MAT above freezing in the Oligocene and the very presence of plants and soils bacteria indicates that an ice sheet did not cover the entire continent. The mismatch between reconstructed ice and the modelled ice/no ice scenario explains the large proxy-model RMSE for the EOT MATs (**Figure 4**). We would also like to note that the ice sheet extent affects catchment sourcing. In this study, we defined source areas with basic polygons on the continent to represent the catchment area from which terrestrial proxies (e.g., soil biomarkers and rock weathering proxies) are exported to marginal marine settings. With the presence of a large ice sheet, soil and plant derived temperature proxies would be limited to unglaciated areas. However, detailed spatial ice sheet reconstructions are unavailable. Thus, for the purposes of this comparison, the source areas were chosen based on drainage basin, proxy type, and estimated ice sheet extent for the model runs.

4.3. Declining pCO_2

Based on the proxy-model comparison it is clear that the lowest RMSE for the Eocene occurs at higher pCO_2 (>560 ppmv) which is in line with previous estimates of pCO_2 suggesting a late Eocene pCO_2 of 830 to 980ppmv from boron and alkenone isotopes (Rae et al., 2021). Previous global proxy model comparison suggest a 40% decrease in pCO_2 across the EOT (Hutchinson et al., 2021), attributed to the lack of dynamic ice sheets and under sensitivity to CO_2 forcing (Hutchinson et al., 2021). The absolute

565 pCO_2 levels are uncertain in the past, due to factors such as boron isotope seawater uncertainties;
566 however, the boron isotope is better at assessing relative change (Raitzsch & Hönisch, 2013). For the
567 alkenone pCO_2 estimates, uncertainties derive from the "b" parameter associated with growth rate and
568 diffusion (Zhang et al., 2020) as well as the effects of irradiance on the carbon isotope fractionation
569 (Phelps et al., 2021). The boron and alkenone isotopes are well studied for the EOT and have a high
570 amount of data relative to other pCO_2 proxies. Current estimates of EOT pCO_2 changes from alkenone
571 $\delta^{13}C$ and boron isotopes suggest a decrease of 140 to 150 ppmv, or roughly 25% (Rae et al., 2021). The
572 best fits between the proxies and model runs for the change in temperature, both MAT and SST, and
573 across all the models (**Table S1 and Figure 5**) suggest a 19-30% decrease in pCO_2 for MAT and 21-46%
574 decrease for SST after exclusion of Site 511 BAYSPLINE. The percent decrease is higher than previous
575 pCO_2 proxy estimates of 16% decrease from boron isotopes (Anagnostou et al., 2016, 2020; Henehan et
576 al., 2020; Pearson et al., 2009) but similar to the estimated 27% decreases from alkenones (Pagani et al.,
577 2005, 2011). The total amount (200-243 ppmv) from the proxy-model comparison is within plausible
578 range of proxy uncertainties. Given that the prescribed post-EOT level was 560 ppmv for the calculations
579 the total amount may vary; however, the percent change is more comparable to pCO_2 records. The pCO_2
580 range falls within estimate from pCO_2 proxies. The discrepancy between the scaling and pCO_2 proxies
581 could be due to additional forcing from ice-albedo feedbacks associated with the presence of an ice sheet,
582 sea ice (both likely) and/or changes in paleogeography. Paleogeography differences between models
583 includes topography differences arising from boundary conditions informed by paleo-elevation
584 reconstructions for the late Eocene/early Oligocene (Baatsen et al., 2020; Goldner et al., 2014;
585 Hutchinson et al., 2018; Kennedy et al., 2015; Ladant et al., 2014a, 2014b; Z. Zhang et al., 2012, 2014),
586 and in some cases ice sheet boundary conditions derived from modern estimates of Antarctic ice volume
587 (e.g. Goldner et al., 2014). Differences arise due to variations in paleogeographic reconstructions,
588 differences in time periods, and choices around ocean gateways (see Table 3). Furthermore, variations in
589 model grid resolution and interpolation methods, which inevitably include arbitrary choices made by each
590 modelling group, also contribute to differences in Antarctic topography. The variations in topographic

591 boundary conditions contribute up to 9°C offsets in absolute MAT computed for the source areas of the
592 land proxies. However, topographic variations remain the same when calculating the temperature
593 anomalies associated with EOT cooling between two simulations of the same model and hence
594 topography.

595 **4.4. Paleogeography with declining pCO_2**

596 While the proxy evidence for SST change fits the expected pCO_2 forcing across the Antarctic region,
597 paleogeography could additionally affect regional patterns of cooling. To evaluate the effects of ocean
598 gateways we used the three models with large paleogeographic changes (UViC, CESM_H and FOAM) to
599 derive a temperature anomaly, denoted T_{GEOG}. Note, that T_{GEOG} is calculate from individual models only,
600 not an ensemble of the three models. For each model (UViC, CESM_H and FOAM), we combined this
601 anomaly with the temperature anomaly due to pCO_2 forcing (**Figure S10a**) from the whole ensemble,
602 denoted T_{CO2}, and used adjustable scaling factors α to find a temperature anomaly ΔT to best fit to the
603 proxy data:

604 $$\Delta T = \alpha(T_{CO2} + T_{GEOG}) \quad (2)$$

605 By scaling α, we derive a decrease in pCO_2 needed to best fit the proxy data (**Figure S10b, c, d, Table**
606 **S4**). We excluded alkenone data from Site 511 which was anomalously cold as previously noted. The
607 UViC model pre-EOT run has both the Drake Passage and Tasman Gateway closed while in the post-
608 EOT run both the Drake Passage and Tasman Gateway are open. The CESM_H model run has the
609 Tasman Gateway open post-EOT while the FOAM run models changes the surface area of West
610 Antarctica. With the addition of the UViC model, the model ensemble mean pCO_2 decrease needed is
611 19.9% with an RMSE of 1.66°C. With the inclusion of CESM_H, the decrease in pCO_2 is 30.3% with an
612 RMSE of 1.0°C. With the inclusion of FOAM, the decrease in pCO_2 is 23.2% with an RMSE of 0.95°C.
613 The inclusion of the paleogeographic runs increases the ΔRMSE from 0.0 to ~0.7°C, which is not
614 significant. However, there is a clear change in the rescaled experiments in the amount of pCO_2 needed to
615 drive the transition. The lower pCO_2 decrease, needed for the EOT with these model simulations, is

consistent with the theory that the gateways opening around Antarctica were part of the explanation for the changes in regional SSTs.

4.5. Implications for future work

4.5.1. Additional southern hemisphere proxy records

The proxy-model temperature comparison identifies the need for an increase in proxy data spatial coverage for the following reasons: to further constrain the uncertainties on the magnitude of the EOT change, to assess proxy-proxy discrepancies, and to identify how paleogeography drives SST heterogeneity in the Southern Ocean. In the EOT proxy-model comparison we acknowledge a limited number of SST and MAT proxy sites (n=6) in the high southern latitudes with most of the records clustered within a few regions. These limited spatial coverage affects the uncertainty and proxy-model comparisons could be more robustly tested with additional sites with proxy reconstructions. On the continent, the availability of additional archives is limited to sites with accessible, outcropping sediments of suitable age, and the modern ice cover is the main impediment. Geological field prospecting for available sediments is the way to see what is possible in terms of adding more MAT estimates and a model-based approach would not be very fruitful to guide land sampling given accessibility limitations, although might help with prioritizing marine margin sites for terrestrial reconstruction. In the open oceans, sediment is in theory deposited everywhere, though water depth and other conditions do limit the availability of SST proxies in some instances (whether through production or preservation). However, there remains great potential to add spatial coverage to proxy SST data and evaluate whether additional proxy records would decrease the proxy-model RMSE. Climate model experiments can help to target marine sampling efforts including guides to the optimal number and locations to drill. Here we demonstrated how an increasing number of sites can reduce the uncertainty of proxy-model SST comparison RMSE, in **Section 4.1.** Beyond the high latitude focus of this study, there is also a dearth of proxy data across the southern hemisphere (especially 20-50ºS) and Hutchinson et al., (2021), called for

more southern hemisphere coverage to enable reconstructions and model comparisons of continental climate and changes in ocean temperature and circulation.

4.5.2. Reducing model discrepancy

While sparse, proxy data contrasts with the global coverage of climate modelled data, and visibly limits proxy-model temperature comparisons, the lack of improvement when performing synthetic comparisons using additional grid cells for the model inter-comparison reveals that model-model disagreement is the major limiting factor in proxy-model comparisons. While additional proxy records would increase the density of evidence for past climates, and these additional proxy data may improve the robustness of proxy-proxy comparisons, this is not the main driver of the uncertainty (RMSE) in proxy-model comparisons at present. Our analysis identifies the primary source of uncertainty is within the model ensemble. We note that this study made use of existing model simulations that were not originally designed for model inter-comparison and therefore did not use the same forcing and boundary conditions. The resulting differences between the simulations result from the differing model physics as well as boundary conditions. While this approach has the advantage of sampling the impact of both model physics and boundary condition uncertainty, future experiments could be designed to better test the comparability of the climate models and the suitability of different boundary conditions in a coordinated way (e.g. DeepMIP-Eocene; Lunt et al., 2021). The priorities for the research questions pursued here would be to address discrepancies in the temperature estimates among the model ensemble as well as the uncertainty surrounding estimation of the pCO_2 decrease needed to force the climate transition of the EOT.

5 Conclusions

The synthesis of recent paleoenvironmental proxy evidence from the high southern latitudes and detailed comparison to regional patterns in climate model experiments allows a new perspective on Antarctic-proximal changes across the EOT. We find spatially heterogeneous cooling of 0 to 3°C (SSTs) and 0 to 4°C (MAT) on land. However, no data are available for the late Eocene and early Oligocene from the

Bellingshausen and Amundsen Seas, or adjacent landmasses. Climate model experiments with prescribed ice sheets lead to localized cooling exceeding that recorded by Oligocene proxies. Our comparison supports higher pCO_2 estimates (>800 ppmv) for the late Eocene to match late Eocene temperature proxies. We compared proxy records to model outputs that assessed a decline in pCO_2, changes in paleogeography, and the addition of a near or above modern size ice sheet. We use these various model experiments to estimate the decline in pCO_2 across the transition that provides the best fit to proxy records from the Antarctic across the Eocene-Oligocene Transition. The decline in MAT and SST from the new proxy compilation was used to scale the multi-model ensemble suggesting a 30 to 33% decrease in pCO_2 similar to recent pCO_2 compilations (Rae et al., 2021). This is encouraging as it suggests that the proxy and climate model data on temperature, pCO_2 and sensitivity may be converging on the magnitude of the pCO_2 forcing of the EOT. However, we caution that inter-model divergence remains the largest source of uncertainty in proxy-model comparisons.

Acknowledgements

We declare no financial conflicts of interests for any author or their affiliations. This research was funded by the U.S. National Science Foundation AGS-1844380 to NJB and OPP-1908548 to SJF. This work resulted from the GeoMeetsClimate MIP internship for EJT at GMU directed by NJB. DKH was supported by Australian Research Council grant DE220100279. Thanks to Scott Knapp for technical assistance to EJT with coding. Thanks to the various modeling and proxy groups that had made their data publicly accessible or fulfilled requests for data or metadata.

Open Research

The proxy compilation is available at Zenodo (Tibbett et al., 2022a). The code notebooks used to perform the analysis and make the figures are available on GitHub (Tibbett et al., 2022d). The model data used in the intercomparison are available on Zenodo (Hutchinson et al., 2023).

References

689 Amoo, M., Salzmann, U., Pound, M. J., Thompson, N., & Bijl, P. K. (2022). Eocene to Oligocene
690 vegetation and climate in the Tasmanian Gateway region were controlled by changes in ocean
691 currents and pCO_2. *Climate of the Past*, *18*(3), 525–546. https://doi.org/10.5194/cp-18-525-2022
692 Anagnostou, E., John, E. H., Babila, T. L., Sexton, P. F., Ridgwell, A., Lunt, D. J., Pearson, P. N., Chalk,
693 T. B., Pancost, R. D., & Foster, G. L. (2020). Proxy evidence for state-dependence of climate
694 sensitivity in the Eocene greenhouse. *Nature Communications*, *11*(1), 4436.
695 https://doi.org/10.1038/s41467-020-17887-x
696 Anagnostou, E., John, E. H., Edgar, K. M., Foster, G. L., Ridgwell, A., Inglis, G. N., Pancost, R. D., Lunt,
697 D. J., & Pearson, P. N. (2016). Changing atmospheric CO2 concentration was the primary driver
698 of early Cenozoic climate. *Nature*, *533*, 380. https://doi.org/10.1038/nature17423
699 Baatsen, M., von der Heydt, A. S., Huber, M., Kliphuis, M. A., Bijl, P. K., Sluijs, A., & Dijkstra, H. A.
700 (2020). The middle to late Eocene greenhouse climate modelled using the CESM 1.0.5. *Climate*
701 *of the Past*, *16*(6), 2573–2597. https://doi.org/10.5194/cp-16-2573-2020
702 Bohaty, S. M., Zachos, J. C., & Delaney, M. L. (2012a). Foraminiferal Mg/Ca evidence for Southern
703 Ocean cooling across the Eocene–Oligocene transition. *Earth and Planetary Science Letters*,
704 *317–318*, 251–261. https://doi.org/10.1016/j.epsl.2011.11.037
705 Bohaty, S. M., Zachos, J. C., & Delaney, M. L. (2012b). Foraminiferal Mg/Ca evidence for Southern
706 Ocean cooling across the Eocene-Oligocene transition. *Earth and Planetary Science Letters*, *317*,
707 251–261. https://doi.org/10.1016/j.epsl.2011.11.037
708 Brassell, S. C. (2014). Climatic influences on the Paleogene evolution of alkenones. *Paleoceanography*,
709 *29*(3), 255–272. https://doi.org/10.1002/2013PA002576
710 Carter, A., Riley, T. R., Hillenbrand, C.-D., & Rittner, M. (2017). Widespread Antarctic glaciation during
711 the Late Eocene. *Earth and Planetary Science Letters*, *458*, 49–57.
712 https://doi.org/10.1016/j.epsl.2016.10.045
713 Coxall, H. K., Huck, C. E., Huber, M., Lear, C. H., Legarda-Lisarri, A., O'Regan, M., Sliwinska, K. K.,
714 van de Flierdt, T., de Boer, A. M., Zachos, J. C., & Backman, J. (2018). Export of nutrient rich

715 Northern Component Water preceded early Oligocene Antarctic glaciation. *Nature Geoscience*,
716 *11*(3), 190–196. https://doi.org/10.1038/s41561-018-0069-9
717 Coxall, H. K., & Pearson, P. N. (2007). The Eocene-Oligocene transition. *Deep Time Perspectives on*
718 *Climate Change: Marrying the Signal From Computer Models and Biological Proxies*, 351–387.
719 Coxall, H. K., Wilson, P. A., Palike, H., Lear, C. H., & Backman, J. (2005). Rapid stepwise onset of
720 Antarctic glaciation and deeper calcite compensation in the Pacific Ocean. *Nature*, *433*(7021),
721 53–57. https://doi.org/10.1038/nature03135
722 Dalziel, I. W. D., Lawver, L. A., Pearce, J. A., Barker, P. F., Hastie, A. R., Barfod, D. N., Schenke, H.-
723 W., & Davis, M. B. (2013). A potential barrier to deep Antarctic circumpolar flow until the late
724 Miocene? *Geology*, *41*(9), 947–950. https://doi.org/10.1130/G34352.1
725 De Jonge, C., Hopmans, E. C., Zell, C. I., Kim, J.-H., Schouten, S., & Sinninghe Damsté, J. S. (2014).
726 Occurrence and abundance of 6-methyl branched glycerol dialkyl glycerol tetraethers in soils:
727 Implications for palaeoclimate reconstruction. *Geochimica et Cosmochimica Acta*, *141*, 97–112.
728 https://doi.org/10.1016/j.gca.2014.06.013
729 Dearing Crampton-Flood, E., Tierney, J. E., Peterse, F., Kirkels, F. M. S. A., & Sinninghe Damsté, J. S.
730 (2020). BayMBT: A Bayesian calibration model for branched glycerol dialkyl glycerol tetraethers
731 in soils and peats. *Geochimica et Cosmochimica Acta*, *268*, 142–159.
732 https://doi.org/10.1016/j.gca.2019.09.043
733 DeConto, R. M., & Pollard, D. (2003). Rapid Cenozoic glaciation of Antarctica induced by declining
734 atmospheric CO2. *Nature*, *421*(6920), 245–249. https://doi.org/10.1038/nature01290
735 Deng, L., Jia, G., Jin, C., & Li, S. (2016). Warm season bias of branched GDGT temperature estimates
736 causes underestimation of altitudinal lapse rate. *Organic Geochemistry*, *96*, 11–17.
737 https://doi.org/10.1016/j.orggeochem.2016.03.004
738 Douglas, P. M. J., Affek, H. P., Ivany, L. C., Houben, A. J. P., Sijp, W. P., Sluijs, A., Schouten, S., &
739 Pagani, M. (2014). Pronounced zonal heterogeneity in Eocene southern high-latitude sea surface

740 temperatures. *Proceedings of the National Academy of Sciences*, *111*(18), 6582.
741 https://doi.org/10.1073/pnas.1321441111
742 Elsworth, G., Galbraith, E., Halverson, G., & Yang, S. (2017). Enhanced weathering and CO2 drawdown
743 caused by latest Eocene strengthening of the Atlantic meridional overturning circulation. *Nature*
744 *Geoscience*, *10*(3), 213–216. https://doi.org/10.1038/ngeo2888
745 Francis, J. E., Marenssi, S., Levy, R., Hambrey, M., Thorn, V. C., Mohr, B., Brinkhuis, H., Warnaar, J.,
746 Zachos, J., Bohaty, S., & DeConto, R. (2008). Chapter 8 From Greenhouse to Icehouse – The
747 Eocene/Oligocene in Antarctica. In F. Florindo & M. Siegert (Eds.), *Developments in Earth and*
748 *Environmental Sciences* (Vol. 8, pp. 309–368). Elsevier. https://doi.org/10.1016/S1571-
749 9197(08)00008-6
750 Fyke, J. G., D'Orgeville, M., & Weaver, A. J. (2015). Drake Passage and Central American Seaway
751 controls on the distribution of the oceanic carbon reservoir. *Global and Planetary Change*, *128*,
752 72–82. https://doi.org/10.1016/j.gloplacha.2015.02.011
753 Galeotti, S., DeConto, R., Naish, T., Stocchi, P., Florindo, F., Pagani, M., Barrett, P., Bohaty, S. M.,
754 Lanci, L., Pollard, D., Sandroni, S., Talarico, F. M., & Zachos, J. C. (2016). Antarctic Ice Sheet
755 variability across the Eocene-Oligocene boundary climate transition. *Science*, *352*(6281), 76.
756 https://doi.org/10.1126/science.aab0669
757 Ghosh, P., Adkins, J., Affek, H., Balta, B., Guo, W., Schauble, E. A., Schrag, D., & Eiler, J. M. (2006).
758 13C–18O bonds in carbonate minerals: A new kind of paleothermometer. *Geochimica et*
759 *Cosmochimica Acta*, *70*(6), 1439–1456. https://doi.org/10.1016/j.gca.2005.11.014
760 Goldner, A., Herold, N., & Huber, M. (2014). Antarctic glaciation caused ocean circulation changes at the
761 Eocene–Oligocene transition. *Nature*, *511*(7511), 574–577. https://doi.org/10.1038/nature13597
762 Gradstein, F. M., Ogg, J. G., Schmitz, M. B., & Ogg, G. M. (2012). *The geologic time scale 2012*.
763 elsevier.

764 Harbert, R. S., & Nixon, K. C. (2015). Climate reconstruction analysis using coexistence likelihood
765 estimation (CRACLE): A method for the estimation of climate using vegetation. *American*
766 *Journal of Botany*, *102*(8), 1277–1289. https://doi.org/10.3732/ajb.1400500
767 Hartman, J. D., Sangiorgi, F., Salabarnada, A., Peterse, F., Houben, A. J. P., Schouten, S., Brinkhuis, H.,
768 Escutia, C., & Bijl, P. K. (2018). Paleoceanography and ice sheet variability offshore Wilkes
769 Land, Antarctica – Part 3: Insights from Oligocene–Miocene TEX_{86}-based sea surface
770 temperature reconstructions. *Climate of the Past*, *14*(9), 1275–1297. https://doi.org/10.5194/cp-
771 14-1275-2018
772 Henderiks, J., & Pagani, M. (2008). Coccolithophore cell size and the Paleogene decline in atmospheric
773 CO2. *Earth and Planetary Science Letters*, *269*(3), 576–584.
774 https://doi.org/10.1016/j.epsl.2008.03.016
775 Henehan, M. J., Edgar, K. M., Foster, G. L., Penman, D. E., Hull, P. M., Greenop, R., Anagnostou, E., &
776 Pearson, P. N. (2020). Revisiting the Middle Eocene Climatic Optimum "Carbon Cycle
777 Conundrum" with new estimates of atmospheric pCO2 from boron isotopes. *Paleoceanography*
778 *and Paleoclimatology*, *35*(6), e2019PA003713.
779 Hollis, C. J., Dunkley Jones, T., Anagnostou, E., Bijl, P. K., Cramwinckel, M. J., Cui, Y., Dickens, G. R.,
780 Edgar, K. M., Eley, Y., Evans, D., Foster, G. L., Frieling, J., Inglis, G. N., Kennedy, E. M.,
781 Kozdon, R., Lauretano, V., Lear, C. H., Littler, K., Lourens, L., … Lunt, D. J. (2019). The
782 DeepMIP contribution to PMIP4: Methodologies for selection, compilation and analysis of latest
783 Paleocene and early Eocene climate proxy data, incorporating version 0.1 of the DeepMIP
784 database. *Geoscientific Model Development*, *12*(7), 3149–3206. https://doi.org/10.5194/gmd-12-
785 3149-2019
786 Hopmans, E. C., Schouten, S., & Sinninghe Damsté, J. S. (2016). The effect of improved chromatography
787 on GDGT-based palaeoproxies. *Organic Geochemistry*, *93*, 1–6.
788 https://doi.org/10.1016/j.orggeochem.2015.12.006

Houben, A. J. P., Bijl, P. K., Sluijs, A., Schouten, S., & Brinkhuis, H. (2019). Late Eocene Southern Ocean Cooling and Invigoration of Circulation Preconditioned Antarctica for Full-Scale Glaciation. *Geochemistry, Geophysics, Geosystems*, *20*(5), 2214–2234. https://doi.org/10.1029/2019GC008182

Houben, A. J. P., van Mourik, C. A., Montanari, A., Coccioni, R., & Brinkhuis, H. (2012). The Eocene–Oligocene transition: Changes in sea level, temperature or both? *Cenozoic Evolution of Antarctic Climates, Oceans and Ice Sheets*, *335–336*, 75–83. https://doi.org/10.1016/j.palaeo.2011.04.008

Hunt, R. J., & Poole, I. (2003). *Paleogene West Antarctic climate and vegetation history in light of new data from King George Island*.

Hutchinson, D. K., Coxall, H. K., Lunt, D. J., Steinthorsdottir, M., de Boer, A. M., Baatsen, M., von der Heydt, A., Huber, M., Kennedy-Asser, A. T., Kunzmann, L., Ladant, J.-B., Lear, C. H., Moraweck, K., Pearson, P. N., Piga, E., Pound, M. J., Salzmann, U., Scher, H. D., Sijp, W. P., … Zhang, Z. (2021). The Eocene–Oligocene transition: A review of marine and terrestrial proxy data, models and model–data comparisons. *Climate of the Past*, *17*(1), 269–315. https://doi.org/10.5194/cp-17-269-2021

Hutchinson, D. K., Coxall, H. K., Lunt, D. J., Steinthorsdottir, M., de Boer, A. M., Baatsen, M., von der Heydt, A., Huber, M., Kennedy-Asser, A. T., Kunzmann, L., Ladant, J.-B., Lear, C. H., Moraweck, K., Pearson, P. N., Piga, E., Pound, M. J., Salzmann, U., Scher, H. D., Sijp, W. P., … Zhang, Z. (2023). Model data archive for a model-data intercomparison of the Eocene-Oligocene transition [Data set]. Zenodo. https://doi.org/10.5281/zenodo.7540322

Hutchinson, D. K., Coxall, H. K., O′Regan, M., Nilsson, J., Caballero, R., & de Boer, A. M. (2019). Arctic closure as a trigger for Atlantic overturning at the Eocene-Oligocene Transition. *Nature Communications*, *10*(1), 3797. https://doi.org/10.1038/s41467-019-11828-z

Hutchinson, D. K., de Boer, A. M., Coxall, H. K., Caballero, R., Nilsson, J., & Baatsen, M. (2018). Climate sensitivity and meridional overturning circulation in the late Eocene using GFDL CM2.1. *Clim. Past*, *14*(6), 789–810. https://doi.org/10.5194/cp-14-789-2018

Kalanetra, K. M., Bano, N., & Hollibaugh, J. T. (2009). Ammonia-oxidizing Archaea in the Arctic Ocean and Antarctic coastal waters. *Environmental Microbiology*, *11*(9), 2434–2445.

Katz, M. E., Miller, K. G., Wright, J. D., Wade, B. S., Browning, J. V., Cramer, B. S., & Rosenthal, Y. (2008). Stepwise transition from the Eocene greenhouse to the Oligocene icehouse. *Nature Geoscience*, *1*(5), 329–334. https://doi.org/10.1038/ngeo179

Kennedy, A. T., Farnsworth, A., Lunt, D. J., Lear, C. H., & Markwick, P. J. (2015). Atmospheric and oceanic impacts of Antarctic glaciation across the Eocene–Oligocene transition. *Philosophical Transactions of the Royal Society A: Mathematical, Physical and Engineering Sciences*, *373*(2054), 20140419. https://doi.org/10.1098/rsta.2014.0419

Kennedy-Asser, A. T., Lunt, D. J., Valdes, P. J., Ladant, J.-B., Frieling, J., & Lauretano, V. (2020). Changes in the high-latitude Southern Hemisphere through the Eocene–Oligocene transition: A model–data comparison. *Climate of the Past*, *16*(2), 555–573. https://doi.org/10.5194/cp-16-555-2020

Kennett, J. P. (1977). Cenozoic evolution of Antarctic glaciation, the circum-Antarctic Ocean, and their impact on global paleoceanography. *Journal of Geophysical Research (1896-1977)*, *82*(27), 3843–3860. https://doi.org/10.1029/JC082i027p03843

Ladant, J.-B., Donnadieu, Y., & Dumas, C. (2014a). Links between CO2, glaciation and water flow: Reconciling the Cenozoic history of the Antarctic Circumpolar Current. *Clim. Past*, *10*(6), 1957–1966. https://doi.org/10.5194/cp-10-1957-2014

Ladant, J.-B., Donnadieu, Y., Lefebvre, V., & Dumas, C. (2014b). The respective role of atmospheric carbon dioxide and orbital parameters on ice sheet evolution at the Eocene-Oligocene transition. *Paleoceanography*, *29*(8), 810–823. https://doi.org/10.1002/2013PA002593

Lauretano, V., Kennedy-Asser, A. T., Korasidis, V. A., Wallace, M. W., Valdes, P. J., Lunt, D. J., Pancost, R. D., & Naafs, B. D. A. (2021). Eocene to Oligocene terrestrial Southern Hemisphere cooling caused by declining pCO2. *Nature Geoscience*, *14*(9), 659–664. https://doi.org/10.1038/s41561-021-00788-z

841 Lear, C. H., Bailey, T. R., Pearson, P. N., Coxall, H. K., & Rosenthal, Y. (2008). Cooling and ice growth
842 across the Eocene-Oligocene transition. *Geology*, *36*(3), 251–254.
843 https://doi.org/10.1130/G24584A.1
844 Liu, Z., Pagani, M., Zinniker, D., DeConto, R., Huber, M., Brinkhuis, H., Shah, S. R., Leckie, R. M., &
845 Pearson, A. (2009). Global Cooling During the Eocene-Oligocene Climate Transition. *Science*,
846 *323*(5918), 1187. https://doi.org/10.1126/science.1166368
847 Lunt, D. J., Bragg, F., Chan, W.-L., Hutchinson, D. K., Ladant, J.-B., Morozova, P., Niezgodzki, I.,
848 Steinig, S., Zhang, Z., Zhu, J., Abe-Ouchi, A., Anagnostou, E., de Boer, A. M., Coxall, H. K.,
849 Donnadieu, Y., Foster, G., Inglis, G. N., Knorr, G., Langebroek, P. M., … Otto-Bliesner, B. L.
850 (2021). DeepMIP: model intercomparison of early Eocene climatic optimum (EECO) large-scale
851 climate features and comparison with proxy data. *Climate of the Past*, *17*(1), 203–227.
852 https://doi.org/10.5194/cp-17-203-2021
853 M. McKay, R., Escutia, C., De Santis, L., Donda, F., Duncan, B., Gohl, K., Gulick, S., Hernández-
854 Molina, J., Hillenbrand, C.-D., Hochmuth, K., Kim, S., Kuhn, G., Larter, R., Leitchenkov, G., H.
855 Levy, R., R. Naish, T., O'Brien, P., F. Pérez, L., E. Shevenell, A., & Williams, T. (2022). Chapter
856 3—Cenozoic history of Antarctic glaciation and climate from onshore and offshore studies. In F.
857 Florindo, M. Siegert, L. D. Santis, & T. Naish (Eds.), *Antarctic Climate Evolution (Second*
858 *Edition)* (pp. 41–164). Elsevier. https://doi.org/10.1016/B978-0-12-819109-5.00008-6
859 Macphail, M. K., & Truswell, E. M. (2004). Palynology of Neogene slope and rise deposits from ODP
860 Sites 1165 and 1167, East Antarctica. *Proceedings of the Ocean Drilling Program. Scientific*
861 *Results*, *188*, 1–20.
862 Miller, K. G., Browning, J. V., Schmelz, W. J., Kopp, R. E., Mountain, G. S., & Wright, J. D. (2020).
863 Cenozoic sea-level and cryospheric evolution from deep-sea geochemical and continental margin
864 records. *Science Advances*, *6*(20), eaaz1346. https://doi.org/10.1126/sciadv.aaz1346
865 Müller, R. D., Cannon, J., Qin, X., Watson, R. J., Gurnis, M., Williams, S., Pfaffelmoser, T., Seton, M.,
866 Russell, S. H. J., & Zahirovic, S. (2018). GPlates: Building a Virtual Earth Through Deep Time.

867 *Geochemistry, Geophysics, Geosystems*, *19*(7), 2243–2261.
868 https://doi.org/10.1029/2018GC007584
869 Naafs, B. D. A., Inglis, G. N., Zheng, Y., Amesbury, M. J., Biester, H., Bindler, R., Blewett, J., Burrows,
870 M. A., del Castillo Torres, D., Chambers, F. M., Cohen, A. D., Evershed, R. P., Feakins, S. J.,
871 Gałka, M., Gallego-Sala, A., Gandois, L., Gray, D. M., Hatcher, P. G., Honorio Coronado, E. N.,
872 … Pancost, R. D. (2017). Introducing global peat-specific temperature and pH calibrations based
873 on brGDGT bacterial lipids. *Geochimica et Cosmochimica Acta*, *208*, 285–301.
874 https://doi.org/10.1016/j.gca.2017.01.038
875 Pagani, M., Huber, M., Liu, Z., Bohaty, S. M., Henderiks, J., Sijp, W., Krishnan, S., & DeConto, R. M.
876 (2011). The Role of Carbon Dioxide During the Onset of Antarctic Glaciation. *Science*,
877 *334*(6060), 1261. https://doi.org/10.1126/science.1203909
878 Pagani, M., Zachos, J. C., Freeman, K. H., Tipple, B., & Bohaty, S. (2005). Marked Decline in
879 Atmospheric Carbon Dioxide Concentrations During the Paleogene. *Science*, *309*(5734), 600.
880 https://doi.org/10.1126/science.1110063
881 Passchier, S., Bohaty, S. M., Jimenez-Espejo, F. J., Pross, J., Roehl, U., van de Flierdt, T., Escutia, C., &
882 Brinkhuis, H. (2013). Early Eocene to middle Miocene cooling and aridification of East
883 Antarctica. *Geochemistry Geophysics Geosystems*, *14*(5), 1399–1410.
884 https://doi.org/10.1002/ggge.20106
885 Passchier, S., Ciarletta, D. J., Miriagos, T. E., Bijl, P. K., & Bohaty, S. M. (2017). An Antarctic
886 stratigraphic record of stepwise ice growth through the Eocene-Oligocene transition. *Geological*
887 *Society of America Bulletin*, *129*(3–4), 318–330. https://doi.org/10.1130/B31482.1
888 Paxman, G. J. G., Jamieson, S. S. R., Ferraccioli, F., Bentley, M. J., Ross, N., Armadillo, E., Gasson, E.
889 G. W., Leitchenkov, G., & DeConto, R. M. (2018). Bedrock Erosion Surfaces Record Former
890 East Antarctic Ice Sheet Extent. *Geophysical Research Letters*, *45*(9), 4114–4123.
891 https://doi.org/10.1029/2018GL077268

892 Paxman, G. J. G., Jamieson, S. S. R., Hochmuth, K., Gohl, K., Bentley, M. J., Leitchenkov, G., &
893 Ferraccioli, F. (2019). Reconstructions of Antarctic topography since the Eocene–Oligocene
894 boundary. *Palaeogeography, Palaeoclimatology, Palaeoecology*, *535*, 109346.
895 https://doi.org/10.1016/j.palaeo.2019.109346
896 Pearson, P. N., Foster, G. L., & Wade, B. S. (2009). Atmospheric carbon dioxide through the Eocene–
897 Oligocene climate transition. *Nature*, *461*(7267), 1110–1113. https://doi.org/10.1038/nature08447
898 Petersen, S. V., & Schrag, D. P. (2015). Antarctic ice growth before and after the Eocene-Oligocene
899 transition: New estimates from clumped isotope paleothermometry: Antarctic ice growth at the
900 E/O transition. *Paleoceanography*, *30*(10), 1305–1317. https://doi.org/10.1002/2014PA002769
901 Phelps, S. R., Stoll, H. M., Bolton, C. T., Beaufort, L., & Polissar, P. J. (2021). Controls on Alkenone
902 Carbon Isotope Fractionation in the Modern Ocean. *Geochemistry, Geophysics, Geosystems*,
903 *22*(12), e2021GC009658. https://doi.org/10.1029/2021GC009658
904 Plancq, J., Mattioli, E., Pittet, B., Simon, L., & Grossi, V. (2014). Productivity and sea-surface
905 temperature changes recorded during the late Eocene–early Oligocene at DSDP Site 511 (South
906 Atlantic). *Palaeogeography, Palaeoclimatology, Palaeoecology*, *407*, 34–44.
907 https://doi.org/10.1016/j.palaeo.2014.04.016
908 Poole, I., Cantrill, D., & Utescher, T. (2005). A multi-proxy approach to determine Antarctic terrestrial
909 palaeoclimate during the Late Cretaceous and Early Tertiary. *Palaeogeography,*
910 *Palaeoclimatology, Palaeoecology*, *222*(1), 95–121. https://doi.org/10.1016/j.palaeo.2005.03.011
911 Popp, B. N., Prahl, F. G., Wallsgrove, R. J., & Tanimoto, J. (2006). Seasonal patterns of alkenone
912 production in the subtropical oligotrophic North Pacific. *Paleoceanography*, *21*(1). Scopus.
913 https://doi.org/10.1029/2005PA001165
914 Pound, M. J., & Salzmann, U. (2017). Heterogeneity in global vegetation and terrestrial climate change
915 during the late Eocene to early Oligocene transition. *Scientific Reports*, *7*, 43386.
916 https://doi.org/10.1038/srep43386

Prahl, F. G., & Wakeham, S. G. (1987). Calibration of unsaturation patterns in long-chain ketone compositions for palaeotemperature assessment. *Nature*, *330*(6146), 367–369. https://doi.org/10.1038/330367a0

Rae, J. W. B., Zhang, Y. G., Liu, X., Foster, G. L., Stoll, H. M., & Whiteford, R. D. M. (2021). Atmospheric CO2 over the Past 66 Million Years from Marine Archives. *Annual Review of Earth and Planetary Sciences*, *49*(1), 609–641. https://doi.org/10.1146/annurev-earth-082420-063026

Raitzsch, M., & Hönisch, B. (2013). Cenozoic boron isotope variations in benthic foraminifers. *Geology*, *41*(5), 591–594. https://doi.org/10.1130/G34031.1

Rose, K. C., Ferraccioli, F., Jamieson, S. S. R., Bell, R. E., Corr, H., Creyts, T. T., Braaten, D., Jordan, T. A., Fretwell, P. T., & Damaske, D. (2013). Early East Antarctic Ice Sheet growth recorded in the landscape of the Gamburtsev Subglacial Mountains. *Earth and Planetary Science Letters*, *375*, 1–12. https://doi.org/10.1016/j.epsl.2013.03.053

Sauermilch, I., Whittaker, J. M., Klocker, A., Munday, D. R., Hochmuth, K., Bijl, P. K., & LaCasce, J. H. (2021). Gateway-driven weakening of ocean gyres leads to Southern Ocean cooling. *Nature Communications*, *12*(1), 6465. https://doi.org/10.1038/s41467-021-26658-1

Scher, H. D., Bohaty, S. M., Smith, B. W., & Munn, G. H. (2014). Isotopic interrogation of a suspected late Eocene glaciation. *Paleoceanography*, *29*(6), 628–644. https://doi.org/10.1002/2014PA002648

Scher, H. D., Bohaty, S. M., Zachos, J. C., & Delaney, M. L. (2011). Two-stepping into the icehouse: East Antarctic weathering during progressive ice-sheet expansion at the Eocene–Oligocene transition. *Geology*, *39*(4), 383–386. https://doi.org/10.1130/G31726.1

Scher, H. D., Whittaker, J. M., Williams, S. E., Latimer, J. C., Kordesch, W. E. C., & Delaney, M. L. (2015). Onset of Antarctic Circumpolar Current 30 million years ago as Tasmanian Gateway aligned with westerlies. *Nature*, *523*(7562), 580–583. https://doi.org/10.1038/nature14598

941 Schouten, S., Hopmans, E. C., Schefuß, E., & Damste, J. S. S. (2002). Distributional variations in marine
942 crenarchaeotal membrane lipids: A new tool for reconstructing ancient sea water temperatures?
943 *Earth and Planetary Science Letters*, *204*(1–2), 265–274.
944 Sheldon, N. D., Retallack, G. J., & Tanaka, S. (2002). Geochemical Climofunctions from North American
945 Soils and Application to Paleosols across the Eocene-Oligocene Boundary in Oregon. *The*
946 *Journal of Geology*, *110*(6), 687–696. https://doi.org/10.1086/342865
947 Sheldon, N. D., & Tabor, N. J. (2009). Quantitative paleoenvironmental and paleoclimatic reconstruction
948 using paleosols. *Earth-Science Reviews*, *95*(1), 1–52.
949 https://doi.org/10.1016/j.earscirev.2009.03.004
950 Sijp, W. P., England, M. H., & Toggweiler, J. R. (2009). Effect of Ocean Gateway Changes under
951 Greenhouse Warmth. *Journal of Climate*, *22*(24), 6639–6652.
952 https://doi.org/10.1175/2009JCLI3003.1
953 Sijp, W. P., von der Heydt, A. S., & Bijl, P. K. (2016). Model simulations of early westward flow across
954 the Tasman Gateway during the early Eocene. *Clim. Past*, *12*(4), 807–817.
955 https://doi.org/10.5194/cp-12-807-2016
956 Sikes, E. L., & Volkman, J. K. (1993). Calibration of alkenone unsaturation ratios (Uk'37) for
957 paleotemperature estimation in cold polar waters. *Geochimica et Cosmochimica Acta*, *57*(8),
958 1883–1889. https://doi.org/10.1016/0016-7037(93)90120-L
959 Sikes, E. L., Volkman, J. K., Robertson, L. G., & Pichon, J. J. (1997). Alkenones and alkenes in surface
960 waters and sediments of the Southern Ocean: Implications for paleotemperature estimation in
961 polar regions. *Geochimica Et Cosmochimica Acta*, *61*(7), 1495–1505.
962 https://doi.org/10.1016/S0016-7037(97)00017-3
963 Speelman, E. N., van Kempen, M. M., Barke, J., Brinkhuis, H., Reichart, G.-J., Smolders, A. J., Roelofs,
964 J. G., Sangiorgi, F., de Leeuw, J. W., & Lotter, A. F. (2009). The Eocene Arctic Azolla bloom:
965 Environmental conditions, productivity and carbon drawdown. *Geobiology*, *7*(2), 155–170.

966 Thompson, N., Salzmann, U., López-Quirós, A., Bijl, P. K., Hoem, F. S., Etourneau, J., Sicre, M.-A.,
967 Roignant, S., Hocking, E., Amoo, M., & Escutia, C. (2022). Vegetation change across the Drake
968 Passage region linked to late Eocene cooling and glacial disturbance after the Eocene–Oligocene
969 transition. *Climate of the Past*, *18*(2), 209–232. https://doi.org/10.5194/cp-18-209-2022
970 Tibbett, E. J., Burls, N. J., Hutchinson, D. K., & Feakins, S. J. (2022d). Ejtibbett/EOTproxymodel: Proxy
971 Model Comparison for the Eocene-Oligocene Transition [ComputationalNotebook]. *Zenodo*.
972 https://doi.org/10.5281/zenodo.7254786
973 Tibbett, E. J., Burls, N. J., Hutchinson, D. K., & Feakins, S. J. (2022a). Southern High Latitude
974 Temperature Proxies from the Late Eocene and Early Oligocene [Dataset]. *Zenodo*.
975 https://doi.org/10.5281/zenodo.7254536
976 Tibbett, E. J., Scher, H. D., Warny, S., Tierney, J. E., & Feakins, S. J. (2021b). *Prydz Bay East*
977 *Antarctica, biomarker and pollen, 36-33 million years. NOAA Paleoclimate Database*.
978 https://www.ncdc.noaa.gov/paleo/study/32052
979 Tibbett, E. J., Scher, H. D., Warny, S., Tierney, J. E., Passchier, S., & Feakins, S. J. (2021a). Late Eocene
980 Record of Hydrology and Temperature From Prydz Bay, East Antarctica. *Paleoceanography and*
981 *Paleoclimatology*, *36*(4), e2020PA004204. https://doi.org/10.1029/2020PA004204
982 Tibbett, E. J., Warny, S., Tierney, J. E., Wellner, J. S., & Feakins, S. J. (2022b). Cenozoic Antarctic
983 Peninsula Temperatures and Glacial Erosion Signals From a Multi-Proxy Biomarker Study.
984 *Paleoceanography and Paleoclimatology*, *37*(9), e2022PA004430.
985 https://doi.org/10.1029/2022PA004430
986 Tibbett, E. J., Warny, S., Tierney, J. E., Wellner, J. S., & Feakins, S. J. (2022c). SHALDRIL Antarctic
987 Peninsula, biomarkers, 37-3 million years [Dataset]. *NOAA Paleoclimate Database*.
988 https://www.ncdc.noaa.gov/paleo/study/35613
989 Tierney, J. E., & Tingley, M. P. (2014). A Bayesian, spatially-varying calibration model for the TEX86
990 proxy. *Geochimica et Cosmochimica Acta*, *127*, 83–106.

Tierney, J. E., & Tingley, M. P. (2018). BAYSPLINE: A New Calibration for the Alkenone Paleothermometer. *Paleoceanography and Paleoclimatology*, *33*(3), 281–301. https://doi.org/10.1002/2017PA003201

Toumoulin, A., Donnadieu, Y., Ladant, J.-B., Batenburg, S. J., Poblete, F., & Dupont-Nivet, G. (2020). Quantifying the Effect of the Drake Passage Opening on the Eocene Ocean. *Paleoceanography and Paleoclimatology*, *35*(8), e2020PA003889. https://doi.org/10.1029/2020PA003889

Truswell, E. M., & Macphail, M. K. (2009). Polar forests on the edge of extinction: What does the fossil spore and pollen evidence from East Antarctica say? *Australian Systematic Botany*, *22*(2), 57–106. https://doi.org/10.1071/SB08046

Utescher, T., Bruch, A. A., Erdei, B., François, L., Ivanov, D., Jacques, F. M. B., Kern, A. K., Liu, Y.-S. (C.), Mosbrugger, V., & Spicer, R. A. (2014). The Coexistence Approach—Theoretical background and practical considerations of using plant fossils for climate quantification. *Palaeogeography, Palaeoclimatology, Palaeoecology*, *410*, 58–73. https://doi.org/10.1016/j.palaeo.2014.05.031

Vahlenkamp, M., Niezgodzki, I., De Vleeschouwer, D., Lohmann, G., Bickert, T., & Pälike, H. (2018). Ocean and climate response to North Atlantic seaway changes at the onset of long-term Eocene cooling. *Earth and Planetary Science Letters*, *498*, 185–195. https://doi.org/10.1016/j.epsl.2018.06.031

Van Breedam, J., Huybrechts, P., & Crucifix, M. (2022). Modelling evidence for late Eocene Antarctic glaciations. *Earth and Planetary Science Letters*, *586*, 117532. https://doi.org/10.1016/j.epsl.2022.117532

Volkman, J. K., Eglinton, G., Corner, E. D. S., & Forsberg, T. E. V. (1980). Long-chain alkenes and alkenones in the marine coccolithophorid Emiliania huxleyi. *Phytochemistry*, *19*(12), 2619–2622. https://doi.org/10.1016/S0031-9422(00)83930-8

Weijers, J. W. H., Bernhardt, B., Peterse, F., Werne, J. P., Dungait, J. A. J., Schouten, S., & Sinninghe Damsté, J. S. (2011). Absence of seasonal patterns in MBT–CBT indices in mid-latitude soils.

Geochimica et Cosmochimica Acta, *75*(11), 3179–3190. https://doi.org/10.1016/j.gca.2011.03.015

Weijers, J. W. H., Schouten, S., van den Donker, J. C., Hopmans, E. C., & Sinninghe Damsté, J. S. (2007). Environmental controls on bacterial tetraether membrane lipid distribution in soils. *Geochimica et Cosmochimica Acta*, *71*(3), 703–713. https://doi.org/10.1016/j.gca.2006.10.003

Westerhold, T., Marwan, N., Drury, A. J., Liebrand, D., Agnini, C., Anagnostou, E., Barnet, J. S. K., Bohaty, S. M., Vleeschouwer, D. D., Florindo, F., Frederichs, T., Hodell, D. A., Holbourn, A. E., Kroon, D., Lauretano, V., Littler, K., Lourens, L. J., Lyle, M., Pälike, H., … Zachos, J. C. (2020). An astronomically dated record of Earth’s climate and its predictability over the last 66 million years. *Science*, *369*(6509), 1383–1387. https://doi.org/10.1126/science.aba6853

Willard, D. A., Donders, T. H., Reichgelt, T., Greenwood, D. R., Sangiorgi, F., Peterse, F., Nierop, K. G. J., Frieling, J., Schouten, S., & Sluijs, A. (2019). Arctic vegetation, temperature, and hydrology during Early Eocene transient global warming events. *Global and Planetary Change*, *178*, 139–152. https://doi.org/10.1016/j.gloplacha.2019.04.012

Wilson, D. S., Pollard, D., DeConto, R. M., Jamieson, S. S. R., & Luyendyk, B. P. (2013). Initiation of the West Antarctic Ice Sheet and estimates of total Antarctic ice volume in the earliest Oligocene. *Geophysical Research Letters*, *40*(16), 4305–4309. https://doi.org/10.1002/grl.50797

Zachos, J. C., Quinn, T. M., & Salamy, K. A. (1996). High-resolution (104 years) deep-sea foraminiferal stable isotope records of the Eocene-Oligocene climate transition. *Paleoceanography*, *11*(3), 251–266.

Zhang, Y. G., Henderiks, J., & Liu, X. (2020). Refining the alkenone-pCO2 method II: Towards resolving the physiological parameter ‘b.’ *Geochimica et Cosmochimica Acta*, *281*, 118–134. https://doi.org/10.1016/j.gca.2020.05.002

Zhang, Z., Nisancioglu, K., Bentsen, M., Tjiputra, J., Bethke, I., Yan, Q., Risebrobakken, B., Andersson, C., & Jansen, E. (2012). Pre-industrial and mid-Pliocene simulations with NorESM-L. *Geoscientific Model Development*, *5*(2), 523–533. https://doi.org/10.5194/gmd-5-523-2012

Zhang, Z., Ramstein, G., Schuster, M., Li, C., Contoux, C., & Yan, Q. (2014). Aridification of the Sahara desert caused by Tethys Sea shrinkage during the Late Miocene. *Nature*, *513*(7518), 401–404. https://doi.org/10.1038/nature13705

Figure Captions

Figure 1. Proxy data compiled for Antarctica, the Southern Ocean and the southern high latitudes spanning the Eocene and Oligocene. a) Map depicting location of records used in this study. b) Land surface mean air temperature (MAT) data including BayMBT (Tibbett et al., 2021a, 2022b), pollen climate reconstructions including NLR (Amoo et al., 2022; Francis et al., 2008; Macphail & Truswell, 2004; Passchier et al., 2013; Poole et al., 2005; Thompson et al., 2022; Truswell & Macphail, 2009), S-index (Passchier et al., 2013, 2017), and MBT/CBT (Douglas et al., 2014). c) Sea surface temperature (SST) data from BAYSPAR calibrated TEX_{86} data (Douglas et al., 2014; Hartman et al., 2018; Houben et al., 2019; Lauretano et al., 2021; Pagani et al., 2011), SSTs from BAYSPLINE calibrated $U^{k'}_{37}$ (Houben et al., 2019; Liu et al., 2009; Pagani et al., 2011; Plancq et al., 2014), and Δ_{47} from bivalves (Douglas et al., 2014; Petersen & Schrag, 2015). d) Air temperature anomaly and e) sea surface temperature anomaly for each Southern Ocean sector with data normalized by the respective datasets Eocene mean in standard deviation units (Z scores), combined for each Southern Ocean sector, and then interpolated to a common interval with a spline fit to the data. Only datasets covering the late Eocene and early Oligocene were used for the temperature anomaly plot. f) $\delta^{18}O_{benthic}$ spline (Westerhold et al., 2020) and pCO_2 compiled from $\delta^{11}B$ (blue) and alkenone (red) proxies (Rae et al., 2021).

Figure 2. Southern hemisphere model MAT for the a) Eocene (4x pCO_2), b) Oligocene (2x pCO_2 model runs), and c) the difference across the transition (2x-4x) showing results for the unscaled multi model ensemble mean. The circles correspond to proxy mean annual air temperature records while the dotted areas show the source area used to compare the model temperature to the proxy record. d) The RMSE for pCO_2 model runs for MAT, for individual model mapped output see **Figure S1**. Red lines are the RMSE for each model after the pCO_2 scaling for RMSE values see **Table S1**.

Figure 3. Southern Ocean sea surface temperatures (SST) for the a) Eocene (4x pCO_2), b) Oligocene (2x pCO_2 model runs), and c) the difference across the transition (2x-4x) showing results for the unscaled multi model ensemble mean. The circles correspond to proxy mean annual air temperature records while the dotted areas show the source area used to compare the model temperature to the proxy record. d) Summarizing the RMSE for pCO_2 model runs for SST, for individual model mapped output see **Figure S3**. Red lines are the RMSE for each model after the pCO_2 scaling for RMSE values see **Table S1**.

Figure 4. Summary of average RMSE across the model experiments a) Eocene runs for CO_2 using 4x pCO_2 (**Table 3**), ice runs contain no ice with pCO_2 of 560 ppmv, Eocene paleogeography runs (**Table 3**) b) Oligocene runs for pCO_2 using 2x pCO_2, ice runs containing the model prescribed ice sheet with pCO_2 of 560 ppmv, and Oligocene paleogeography runs c) is the difference model outputs between the Oligocene and Eocene runs. (**Table 3**). The x axis headers correspond as follows: CO_2 distinguishes the proxy-model comparison based on pCO_2 changes, ice for the with and without an ice sheet, and geo for the model runs with paleogeographic changes. MAT and SST correspond to either air or sea surface temperature comparison Mean is the orange line with outliers as dots. The dot outlier is from the GFDL CM2.1 model. Blue line is the ensemble mean from the pCO_2 scaling.

Figure 5. a) Proxy-model ΔMAT comparison after scaling the pCO_2 forcing to achieve best fit to the magnitude of cooling in the proxy MATs, b) Proxy-model ΔSST comparison after scaling the pCO_2

forcing to achieve best fit to the magnitude of cooling in the proxy SSTs. The grey area in the Eocene timeslice identifies the separate source regions used in Prydz Bay based on the proxy type. In the Oligocene run the catchment is restricted on the basis of ice expansion reducing the effective catchment area for Prydz Bay and the Ross Sea. In the Oligocene-Eocene panel the grey panel represents the Eocene area used for Prydz Bay while the line for source region corresponds to proxy sourcing areas for the Oligocene.

Figure 1.

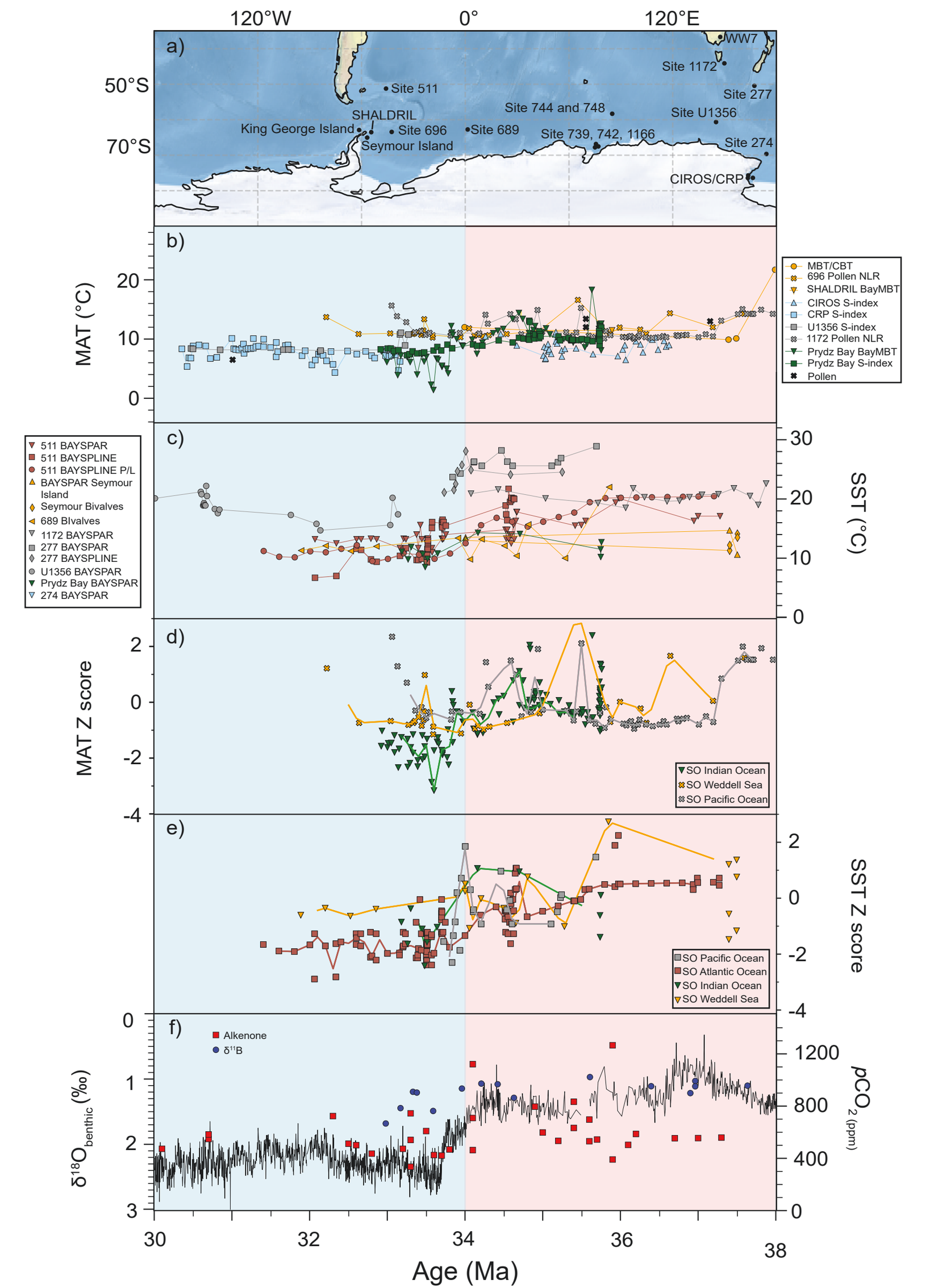
120°W
0°
120°E
a)
50°S
70°S
WW7
Site 1172
Site 277
Site 744 and 748
Site U1356
Site 511
SHALDRIL
King George Island
Site 696
Site 689
Site 739, 742, 1166
Site 274
Seymour Island
CIROS/CRP
b)
MAT (°C)
20
10
0
MBT/CBT
696 Pollen NLR
SHALDRIL BayMBT
CIROS S-index
CRP S-index
U1356 S-index
1172 Pollen NLR
Prydz Bay BayMBT
Prydz Bay S-index
Pollen
c)
511 BAYSPAR
511 BAYSPLINE
511 BAYSPLINE P/L
BAYSPAR Seymour Island
Seymour Bivalves
689 BIvalves
1172 BAYSPAR
277 BAYSPAR
277 BAYSPLINE
U1356 BAYSPAR
Prydz Bay BAYSPAR
274 BAYSPAR
30
20
10
0
SST (°C)
d)
MAT Z score
2
0
-2
-4
SO Indian Ocean
SO Weddell Sea
SO Pacific Ocean
e)
2
0
-2
-4
SST Z score
SO Pacific Ocean
SO Atlantic Ocean
SO Indian Ocean
SO Weddell Sea
f)
Alkenone
δ11B
δ18Obenthic (‰)
0
1
2
3
1200
800
400
0
pCO2 (ppm)
30
32
34
36
38
Age (Ma)

Figure 2.

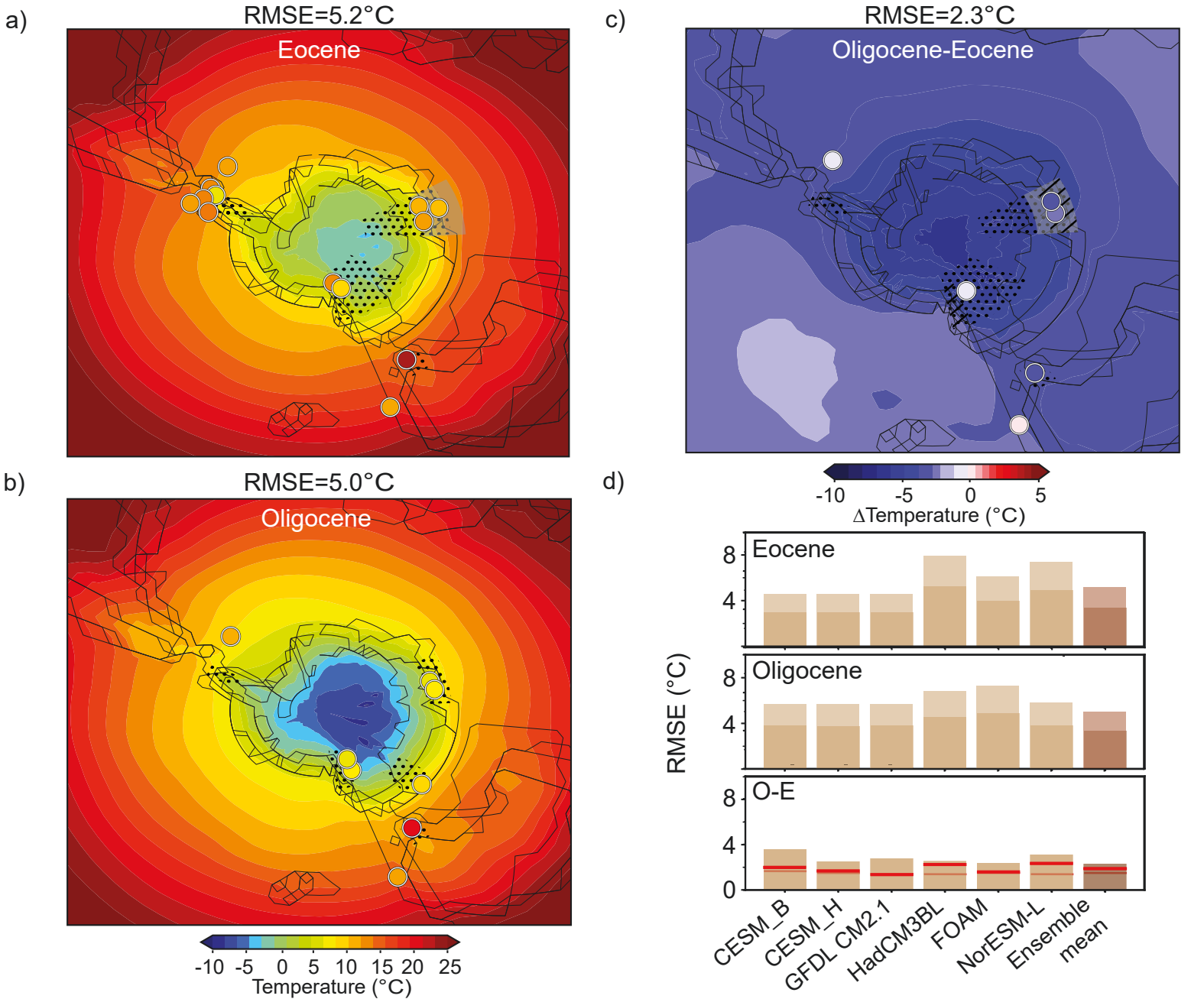
a)
RMSE=5.2°C
Eocene
b)
RMSE=5.0°C
Oligocene
-10 -5 0 5 10 15 20 25
Temperature (°C)
c)
RMSE=2.3°C
Oligocene-Eocene
-10 -5 0 5
ΔTemperature (°C)
d)
RMSE (°C)
Eocene
Oligocene
O-E
8
4
0
CESM_B
CESM_H
GFDL CM2.1
HadCM3BL
FOAM
NorESM-L
Ensemble mean

Figure 3.

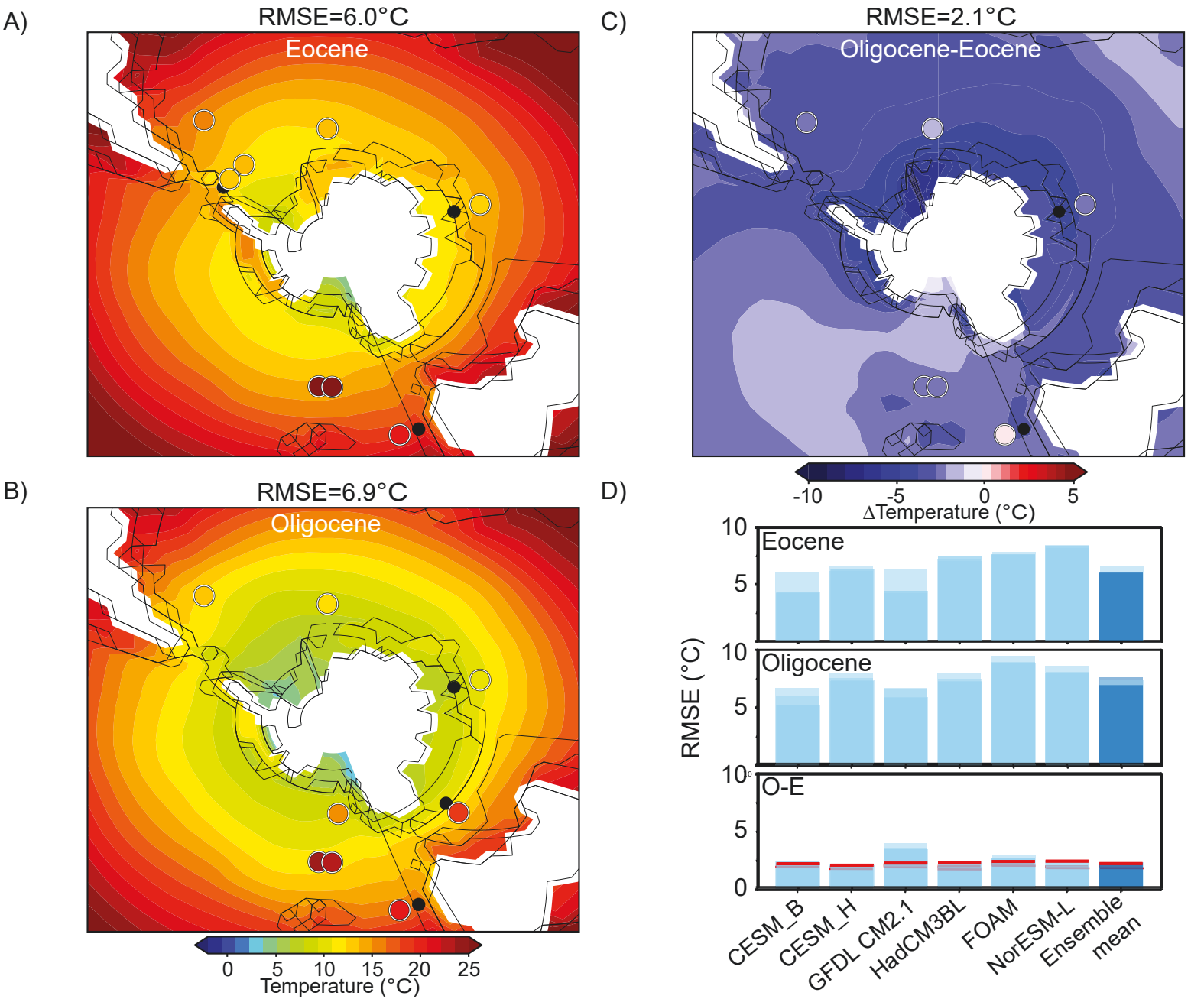
A)
RMSE=6.0°C
Eocene
B)
RMSE=6.9°C
Oligocene
0
5
10
15
20
25
Temperature (°C)
C)
RMSE=2.1°C
Oligocene-Eocene
-10
-5
0
5
ΔTemperature (°C)
D)
RMSE (°C)
Eocene
Oligocene
O-E
10
5
0
CESM_B
CESM_H
GFDL CM2.1
HadCM3BL
FOAM
NorESM-L
Ensemble mean

Figure 4.

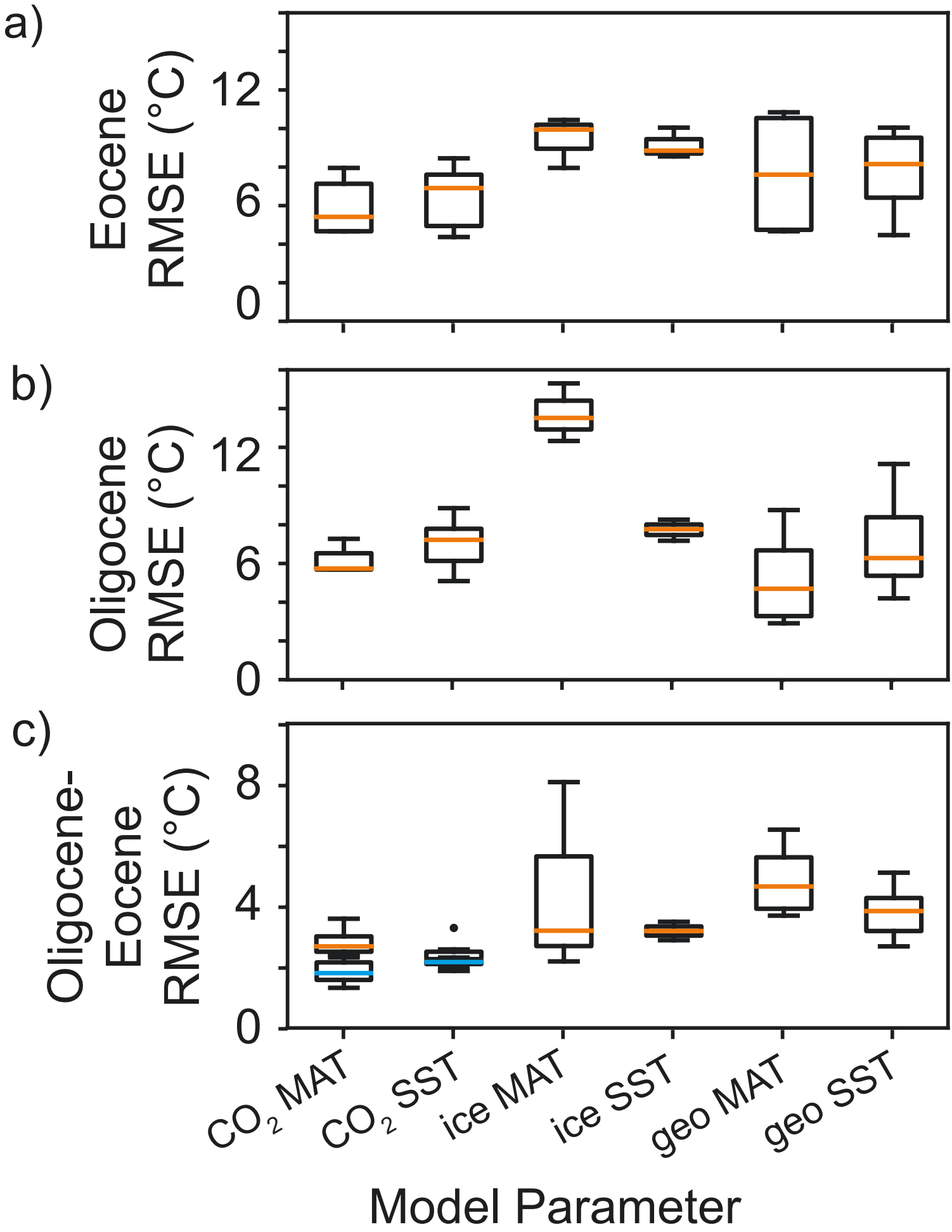
a)
Eocene RMSE (°C)
12
6
0
b)
Oligocene RMSE (°C)
12
6
0
c)
Oligocene-Eocene RMSE (°C)
8
4
0
CO2 MAT
CO2 SST
ice MAT
ice SST
geo MAT
geo SST
Model Parameter

Figure 5.

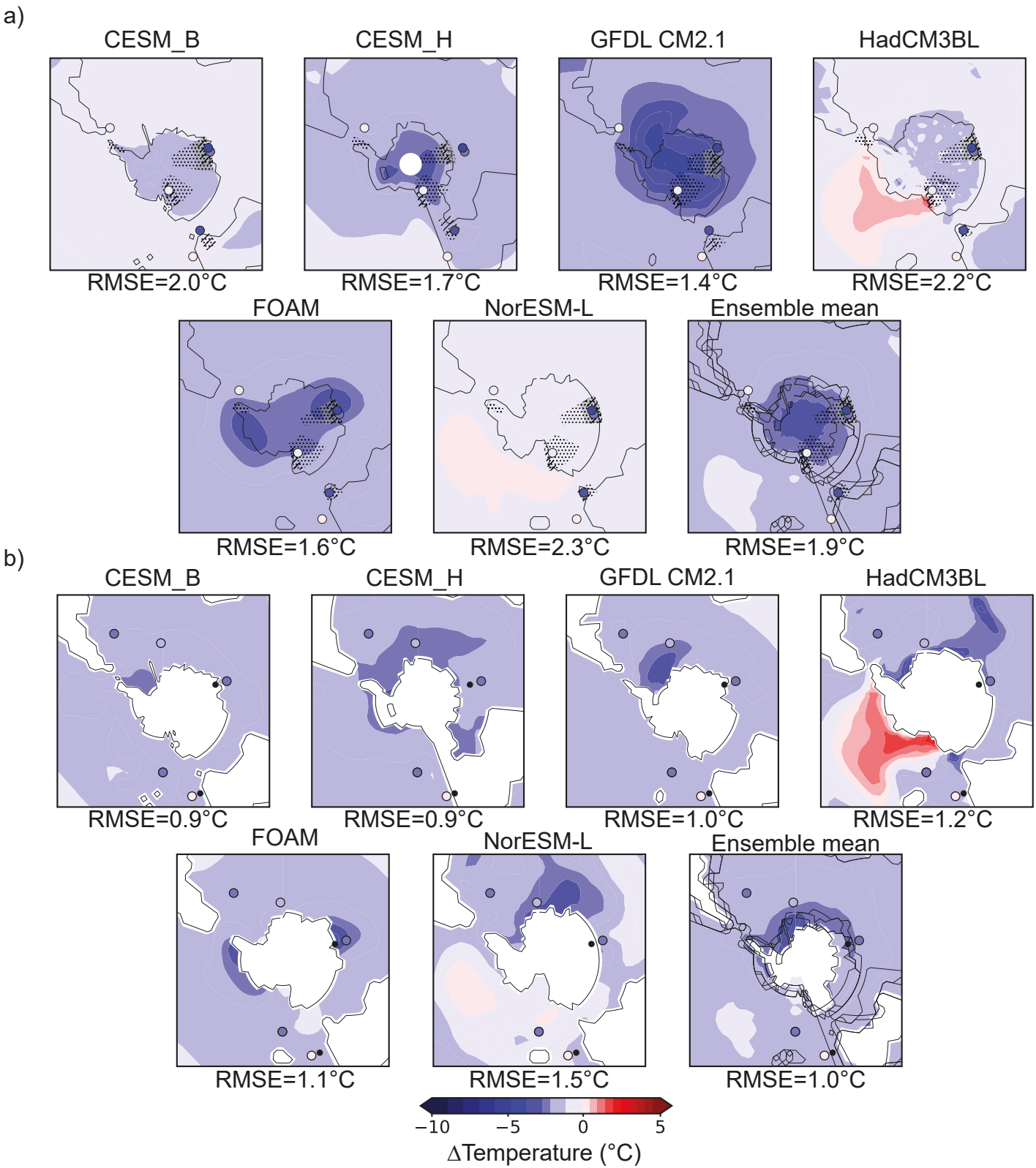
a)
CESM_B
CESM_H
GFDL CM2.1
HadCM3BL
RMSE=2.0°C
RMSE=1.7°C
RMSE=1.4°C
RMSE=2.2°C
FOAM
NorESM-L
Ensemble mean
RMSE=1.6°C
RMSE=2.3°C
RMSE=1.9°C
b)
CESM_B
CESM_H
GFDL CM2.1
HadCM3BL
RMSE=0.9°C
RMSE=0.9°C
RMSE=1.0°C
RMSE=1.2°C
FOAM
NorESM-L
Ensemble mean
RMSE=1.1°C
RMSE=1.5°C
RMSE=1.0°C
−10
−5
0
5
ΔTemperature (°C)